Lawrence Berkeley National Laboratory
LBL Publications

Title
GRB 260310A/SN 2026fgk: Photometric and Spectroscopic Evolution of a Nearby Gamma-Ray Burst Supernova and an Exceptionally Bright Afterglow at z = 0.153

Permalink
https://escholarship.org/uc/item/5x55b8kc

Journal
The Astrophysical Journal, 1006(2)

ISSN
0004-637X

Authors
O'Connor, Brendan
Busmann, Malte
Hall, Xander J
et al.

Publication Date
2026-08-01

DOI
10.3847/1538-4357/ae878f

Copyright Information
This work is made available under the terms of a Creative Commons Attribution License, available at https://creativecommons.org/licenses/by/4.0/

Peer reviewed

eScholarship.org Powered by the California Digital Library
University of California

The Astrophysical Journal, 1006:210 (16pp), 2026 August 1 https://doi.org/10.3847/1538-4357/ae878f
© 2026. The Author(s). Published by the American Astronomical Society.
OPEN ACCESS

GRB 260310A/SN 2026fgk: Photometric and Spectroscopic Evolution of a Nearby Gamma-Ray Burst Supernova and an Exceptionally Bright Afterglow at $z = 0.153$

Brendan O'Connor[1,12], Malte Busmann[2,3], Xander J. Hall[1], Kenta Taguchi[4], Masaomi Tanaka[5,6], Daniel Gruen[2,3], Seiji Toshikage[5], Ariel J. Amsellem[1], Ziyuan Zhu[2], Antonella Palmese[1], Dylan Green[7], John Banovetz[7], Yu-Han Yang[8], Eleonora Troja[8], Hendrik van Eerten[9], Julius Gassert[1,2], Mitra Maleki[2], Stephen Bailey[7], Segev BenZvi[10], Tomás Cabrera[1], Keerthi Kunnumkai[1], Adam D. Myers[11], Christoph Ries[2], David Schlegel[7], Michael Schmidt[2], Silona Wilke[2], and Muskan Yadav[8]

[1] McWilliams Center for Cosmology and Astrophysics, Department of Physics, Carnegie Mellon University, Pittsburgh, PA 15213, USA; boconno2@andrew.cmu.edu
[2] University Observatory, Faculty of Physics, Ludwig-Maximilians-Universität München, Scheinerstraße 1, 81679 Munich, Germany
[3] Excellence Cluster ORIGINS, Boltzmannstraße 2, 85748 Garching, Germany
[4] Department of Astronomy, Kyoto University, Kitashirakawa-Oiwake-cho, Sakyo-ku, Kyoto 606-8502, Japan
[5] Astronomical Institute, Tohoku University, Sendai 980-8578, Japan
[6] Division for the Establishment of Frontier Sciences, Organization for Advanced Studies, Tohoku University, Sendai 980-8577, Japan
[7] Lawrence Berkeley National Laboratory, 1 Cyclotron Road, Berkeley, CA 94720, USA
[8] Dipartimento di Fisica, Università di Tor Vergata, Via della Ricerca Scientifica 1, 00133 Rome, Italy
[9] Department of Physics, University of Bath, Building 3 West, Bath BA2 7AY, UK
[10] Department of Physics & Astronomy, University of Rochester, 206 Bausch and Lomb Hall, P.O. Box 270171, Rochester, NY 14627-0171, USA
[11] Department of Physics & Astronomy, University of Wyoming, 1000 East University, Department 3905, Laramie, WY 82071, USA
Received 2026 May 18; revised 2026 June 23; accepted 2026 June 28; published 2026 July 28

Abstract

The association of broad-lined Type Ic (Ic-BL) supernovae with long-duration gamma-ray bursts (GRBs) has been known for 28 yr. However, only about 70 GRB supernovae (GRB-SNe) have been identified, of which only one-half have spectroscopic classifications. At $z = 0.153$, GRB 260310A is the twelfth spectroscopically confirmed GRB-SN discovered within 1 Gpc, offering a critical opportunity to follow one of these rare supernovae in detail. We present optical to near-infrared imaging and spectroscopy of GRB 260310A and SN 2026fgk out to 65 days after discovery. The optical afterglow is among the brightest ever observed from a GRB. Spectra obtained more than 2 weeks after the explosion reveal broad absorption features that securely identify SN 2026fgk as a Type Ic-BL supernova (SN). Modeling of the multiwavelength (*grizJK*$_s$) lightcurve shows that the SN is approximately one-half the luminosity ($k_{98bw} = 0.4$–0.6) of the canonical GRB-SN 1998bw. We derive a nickel mass of $M_{Ni} = 0.4$–$0.5\,M_\odot$ with a total ejected mass of $M_{ej} \approx 4$–$6\,M_\odot$ and kinetic energy $E_K = (3$–$8) \times 10^{51}$ erg. The GRB exploded at an extremely large offset of 15 kpc from its host galaxy. Long-slit spectra reveal a "bridge" of nebular emission extending along the galaxy's disk to the GRB location, which has a subsolar metallicity ($\sim 0.4\,Z_\odot$), compared to a near-solar metallicity for the host galaxy. This indicates that the large offset arises from the galaxy's extended light profile rather than an isolated environment.

Unified Astronomy Thesaurus concepts: Time domain astronomy (2109); Gamma-ray bursts (629); Relativistic jets (1390); Core-collapse SNe (304); Type Ic SNe (1730)

Materials only available in the online version of record: machine-readable table

1. Introduction

Long-duration gamma-ray bursts (GRBs) are among the most explosive and energetic objects in the Universe. For the past 3 decades, these events have been widely understood to mark the deaths of massive stars. The key observational breakthroughs came first from the association of the low-luminosity GRB 980425 to SN 1998bw (T. J. Galama et al. 1998; K. Iwamoto et al. 1998; S. R. Kulkarni et al. 1998; T. J. Galama et al. 1999; R. A. Stathakis et al. 2000; F. Patat et al. 2001; C. Kouveliotou et al. 2004), and later from the spectroscopic identification of SN 2003dh (J. Hjorth et al. 2003; T. Matheson et al. 2003; P. A. Mazzali et al. 2003; K. Z. Stanek et al. 2003; J. Deng et al. 2005) in the afterglow of the more energetic, cosmological burst GRB 030329 (E. Berger et al. 2003; K. Sheth et al. 2003; Y. M. Lipkin et al. 2004; G. B. Taylor et al. 2004; R. Vanderspek et al. 2004; A. J. van der Horst et al. 2008). These events established that the SNe accompanying long GRBs (GRB-SNe) are typically broad-lined Type Ic (Ic-BL) explosions. These are stripped-envelope core-collapse SNe whose spectra show very broad absorption features (typically Fe II and Si II), implying high ejecta velocities ($>10{,}000$ km s^{-1}) and large kinetic energies (S. E. Woosley & J. S. Bloom 2006; J. Hjorth & J. S. Bloom 2012; J. Hjorth 2013; Z. Cano et al. 2017a). Over the past 2 decades our understanding of GRB-SNe has evolved to include a broader diversity of SN properties, though they tend to a narrow range of luminosities and ejecta properties (e.g., Z. Cano et al. 2017a) that do not appear to correlate with the GRB jet's energetics (e.g, J. Hjorth 2013). To date, there are roughly 70 GRB-SN associations. Roughly one-half of these

[12] McWilliams Fellow.

Original content from this work may be used under the terms of the Creative Commons Attribution 4.0 licence. Any further distribution of this work must maintain attribution to the author(s) and the title of the work, journal citation and DOI.

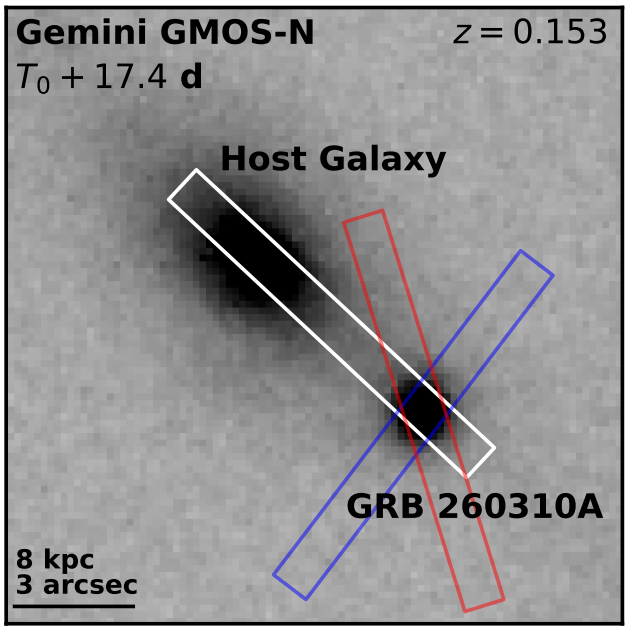


Figure 1. Gemini *r*-band acquisition image (3 × 15 s) from 2026 March 27 ($T_0 + 17.4$ days) showing the placement of the Gemini spectroscopic long-slit (white) observation that covers both the GRB and the host galaxy. Later Gemini spectra were obtained using different position angles (blue for 2026 April 23; red for 2026 May 13). The length of the rectangles mimicking the slit are simply for visualization purposes, while the 1″ width is shown to scale. North is up and east is to the left.

GRB-SNe have spectroscopic classifications (see, e.g., J. Hjorth & J. S. Bloom 2012; Z. Cano et al. 2017a; G. Finneran et al. 2025, and references therein), while the remaining candidates are based on late-time photometric bumps in their optical lightcurves (e.g., J. S. Bloom et al. 1999; A. Zeh et al. 2004).

The association of GRBs to stripped-envelope SNe fits within the collapsar framework for long GRB production (S. E. Woosley 1993; A. I. MacFadyen & S. E. Woosley 1999; A. I. MacFadyen et al. 2001). In this model, the core collapse of a rapidly rotating, stripped star powers both a relativistic jet and an SN. Material falling onto a newly formed black hole, or in some cases a rapidly spinning magnetized compact remnant, launches a jet that drills through the star and produces the prompt gamma-ray emission (see, e.g., T. Piran 2004), while radioactive heating from freshly synthesized ^{56}Ni powers the optical SN (see, e.g., S. E. Woosley & J. S. Bloom 2006; J. Hjorth & J. S. Bloom 2012; Z. Cano et al. 2017a). The observational association between long GRBs and SNe is therefore a cornerstone of our understanding of jet-driven stellar death.

Low-redshift events are especially valuable because they provide the clearest opportunity to disentangle afterglow, host galaxy, and SN light, and to follow the spectroscopic evolution in detail. GRB 260310A is the latest nearby burst to offer this opportunity. The event was detected by Fermi (Fermi GBM Team 2026; R. Hamburg & C. Meegan 2026) and AstroSat (S. Salunke et al. 2026), although the initial localization was poor. An optical counterpart was discovered by GOTO (D. O'Neill et al. 2026) and reported to the Transient Name Server (TNS),[13] and subsequent optical follow-up strengthened its association with GRB 260310A (K. Hinds et al. 2026; R. Konno et al. 2026). The identification was then secured by the discovery of X-ray and radio counterparts (C. T. Christy et al. 2026; S. Giarratana et al. 2026; R. Jayaraman et al. 2026b; L. Rhodes et al. 2026), which established that the optical transient was indeed the afterglow of the burst.

A redshift of $z = 0.153$ was measured from nebular emission lines (A. de Ugarte Postigo et al. 2026b; K.-R. Hinds et al. 2026a; B. Hsu et al. 2026). At this distance, the burst had an isotropic-equivalent gamma-ray energy release of $E_{\gamma,\mathrm{iso}} = 3.5 \times 10^{50}$ erg and a rest-frame spectral peak energy of $E_\mathrm{p} = 200$ keV (J.-L. Atteia et al. 2026; Fermi GBM Team 2026; K.-R. Hinds et al. 2026a), placing it as a significant outlier to the Amati relation (L. Amati et al. 2002; L. Amati 2006). Owing to its proximity, the optical afterglow is one of the brightest ever observed from a GRB (D. A. Perley et al. 2026). At later times, optical spectroscopy revealed the emergence of a Type Ic-BL SN, SN 2026fgk, in the lightcurve (A. de Ugarte Postigo et al. 2026a; R. Gill et al. 2026; K.-R. Hinds et al. 2026b; B. O'Connor et al. 2026b), conclusively linking GRB 260310A to the collapse of a massive stripped star. GRB 260310A/SN 2026fgk is therefore only the twelfth GRB-SN discovered within 1 Gpc. In this paper we present a photometric and spectroscopic characterization of the optical to near-infrared (OIR) afterglow of GRB 260310A and of the associated SN SN 2026fgk, place the event in the context of the known GRB-SN population, and use it to extend the still limited sample of nearby, spectroscopically secure GRB-SNe.

Throughout the manuscript we adopt a standard ΛCDM cosmology (Planck Collaboration et al. 2020) with $H_0 = 67.4\ \mathrm{km\ s^{-1}\ Mpc^{-1}}$, $\Omega_m = 0.315$, and $\Omega_\Lambda = 0.685$. At redshift $z = 0.153$, this cosmology corresponds to a luminosity distance of 756 Mpc. All upper limits are reported at the 3σ level and all magnitudes are in the AB system.

2. Observations

2.1. Fraunhofer Telescope Wendelstein

We observed the OIR counterpart of GRB 260310A with the Three Channel Imager (3KK; F. Lang-Bardl et al. 2016) mounted on the 2.1 m Fraunhofer Telescope at Wendelstein Observatory (FTW; U. Hopp et al. 2014). Observations began on 2026 March 13, corresponding to 3.6 days after the trigger. The 3KK camera is capable of obtaining images in three filters simultaneously: two optical and one near-infrared (NIR). We carried out daily observations in the *griz* bands as weather allowed. NIR observations (JK_s) were initially obtained simultaneously, but were not available after 2026 March 28 due to an issue with the cooling system. The cooling system was repaired and NIR observations began again on 2026 April 22. The complete log of observations is tabulated in Table 1.

The FTW data were reduced using a custom pipeline (C. A. Gössl & A. Riffeser 2002) to perform bias and dark subtraction, flat-fielding, and cosmic-ray rejection. For more details, specifically with regard to the NIR data reduction, see M. Busmann et al. (2025). For optical images, we performed difference imaging with the Saccadic Fast Fourier Transform (SFFT) software[14] (L. Hu et al. 2022) using archival Pan-STARRS1 (K. C. Chambers et al. 2016), hereafter PS1, and Legacy Survey images as templates. Due to the large host offset, the non-difference-imaging photometry was nearly

[13] https://www.wis-tns.org/object/2026fgk

[14] https://github.com/thomasvrussell/sfft

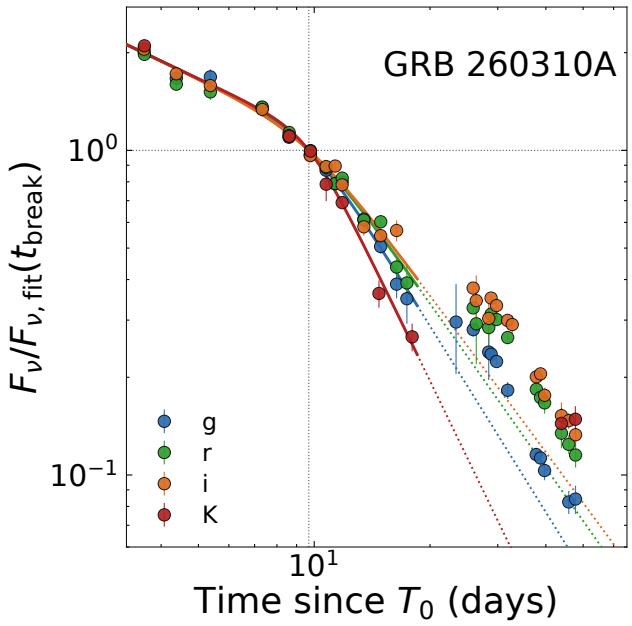


Figure 2. Normalized flux density relative to the flux density at the break time t_{break} for the *griK* bands. This shows the different relative slopes of these bands after the break, as well as the late-time color evolution.

identical (<0.1 mag deviations) to difference imaging photometry until late times ($\gtrsim$15 days). Due to the lack of available NIR templates, the JK_s photometry did not undergo difference imaging. We performed aperture photometry on the difference images using `Photutils` (L. Bradley et al. 2024) with AB magnitude zero-points calibrated to the PS1 (K. C. Chambers et al. 2016) and Two Micron All Sky Survey (M. F. Skrutskie et al. 2006) catalogs for optical and NIR data, respectively. Standard Vega to AB magnitude conversions were applied to the NIR data. The photometry is reported in Table 1.

2.2. Seimei Telescope

We obtained low-resolution spectra at two epochs using the Kyoto Okayama Optical Low-dispersion Spectrograph with optical-fiber integral-field unit (KOOLS-IFU; K. Matsubayashi et al. 2019, 2025), mounted on the 3.8 m Seimei telescope on Mount Chikurinji, Japan. We used VPH-blue (2026 March 14) and VPH-red (2026 March 15) grisms, giving a spectral resolution of $\lambda/\Delta\lambda \simeq 500$ and 700, respectively. After a standard reduction procedure including bias subtraction, flat-field correction, distortion correction, and cosmic-ray removal, a one-dimensional spectrum was extracted from the two-dimensional image by subtracting a sky spectrum extracted from the region around the target. For the wavelength calibration, we used Hg, Ne, and Xe lamp frames. Finally, we performed flux calibration by observing a spectrophotometric standard star (HR3454). A log of spectral observations is presented in Table 2.

We obtained *g*-, *r*-, *i*-, and *z*-band images using the TriColor CMOS Camera and Spectrograph (TriCCS) mounted on the 3.8 m Seimei telescope starting on 2026 March 14. After standard image reduction procedures including bias, dark and flat corrections, and astrometric alignment, the multiple images in each filter taken on the same night are stacked based on the astrometric solution. Difference imaging and photometry was performed using the same pipeline and methods as outlined above for FTW (see Section 2.1). The photometry is reported in Table 1.

2.3. DESI

The Dark Energy Spectroscopic Instrument (DESI) includes of 5000 science fibers that can each be positioned independently on sky (E. F. Schlafly et al. 2023; C. Poppett et al. 2024). Each fiber is 107 μm in diameter, which is equivalent to $\sim$1.″5 on the sky. The spectrograph utilizes three cameras in the approximate *BRZ* bands that cover 3600–9824 Å at a spectral resolution $R \sim$ 2000–5500 (DESI Collaboration et al. 2016, 2025, 2026; T. N. Miller et al. 2024). Each spectrum is reduced and flux calibrated with the DESI spectroscopic data pipeline (J. Guy et al. 2023).

DESI obtained a sequence of spectra of GRB 260310A (see Table 2) at 6.2, 7.1, 8.1, and 12.1 days after the GRB discovery. Each spectrum had an effective DESI exposure of 1200 s as part of a "dark" time tile. The spectra were obtained as part of the DESI Transients Survey (X. J. Hall et al. 2026b), a spare fiber program that targets publicly reported transients. For other examples of DESI spare fiber targets and a more in-depth review of the observing strategy, see A. D. Myers et al. (2023), DESI Collaboration et al. (2024), and X. J. Hall et al. (2026b, 2026c). The DESI spectra are publicly available through the DESI Transients Survey Zenodo (X. J. Hall et al. 2026a). The DESI spectra are automatically corrected for Galactic extinction, which is minimal in this field ($E(B-V) = 0.02$ mag; E. F. Schlafly & D. P. Finkbeiner 2011).

2.4. HET

We observed GRB 260310A with the 11 m Hobby-Eberly Telescope (HET; L. W. Ramsey et al. 1998; G. J. Hill et al. 2021) at McDonald Observatory under program M26-1-005 (PI: D. Gruen) on 2026 March 19). The observations were scheduled using the HET queue-scheduling system (M. Shetrone et al. 2007). We used the low-resolution integral-field spectrograph (LRS2; T. S. Chonis et al. 2014, 2016) to obtain spectra in the red channel (i.e., LRS2-R data). The raw LRS2 data were initially processed with `Panacea`,[15] which performs bias subtraction, dark subtraction, fiber tracing, fiber wavelength evaluation, fiber extraction, fiber-to-fiber normalization, source detection, source extraction, and flux calibration for each channel. The absolute flux calibration was based on default response curves, measurements of mirror illumination, and exposure throughput derived from guider images. We extracted the flux-calibrated one-dimensional spectrum using the `LRS2Multi`[16] package, integrating over the 0.″59 fibers within a 1.″5 radius aperture centered on the transient (Figure 1).

2.5. Gemini

We performed observations with the Gemini Multi-Object Spectrograph (GMOS) at Gemini-North under programs GN-2026A-Q-202 (PI: M. Tanaka), GN-2026A-DD-102 (PI: B. O'Connor), and GN-2026A-Q-123 (PI: G. Srinivasaragavan). The observations were performed under program GN-2026A-DD-102 (PI: B. O'Connor) with the time charged across multiple programs. Long-slit spectroscopy of the optical

[15] https://github.com/grzeimann/Panacea
[16] https://github.com/grzeimann/LRS2Multi

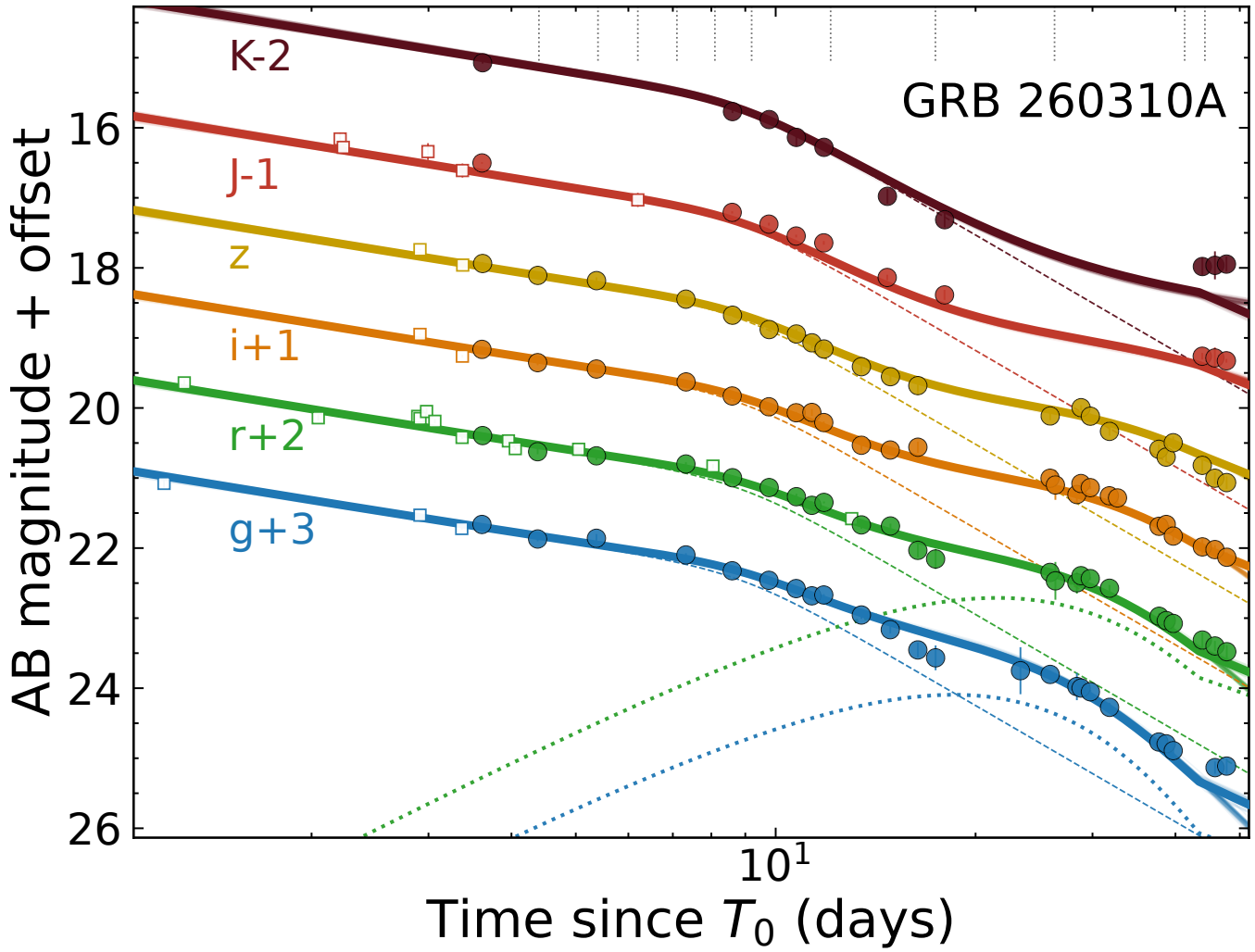


Figure 3. Best-fit model (power law + Arnett) to the multiwavelength lightcurve of GRB 260310A in the observer frame. The thick solid lines in each filter represent the total model. The thin dashed lines represent the broken power-law afterglow component, and the dotted lines, shown only in the *g* and *r* bands to avoid clutter, represents the Arnett model lightcurve. Photometry presented in this work (FTW and Seimei) is shown as solid circles and publicly reported photometry compiled from GCN Circulars is shown as empty squares (S. Belkin & M. Shrestha 2026; R. Brivio et al. 2026; K. Hinds et al. 2026; R. Konno et al. 2026; C.-H. Lai et al. 2026; J.-J. Li et al. 2026; A. Martin-Carrillo et al. 2026a, 2026b; E. Moreno Méndez et al. 2026; N. Passaleva et al. 2026; D. A. Perley et al. 2026; R. Stein et al. 2026; A. M. Watson et al. 2026). The vertical lines at the top of the figure mark the epochs of our optical spectra (Figure 4).

transient was acquired on 2026 March 27 (17.4 days; PIs: M. Tanaka and B. O'Connor), 2026 April 5 (26.3 days) and 2026 April 20 (41.3 days), 2026 April 23 (44.3 days), and 2026 May 13 (64.1 days), see also Table 2. Due to shared data access of the late spectra, these spectra also appear in K.-R. Hinds et al. (2026b). All spectra used the B480 grating and a 1″ slit width. For the spectra taken on 2026 March 27, 2026 April 5, and 2026 April 20, the slit covered both the transient and the host galaxy as shown in Figure 1. These spectra suffer from slit losses caused by atmospheric differential refraction (A. V. Filippenko 1982) and have untrustworthy flux calibrations at the blue end, which we exclude from our analysis. The spectra have been absolute flux calibrated based on near-simultaneous photometry, which agrees with the observed spectral shapes at >5000 Å. Additional corrections for slit losses were made following (A. V. Filippenko 1982). Atmospheric differential refraction does not impact the identification of SN features at >5000 Å. The slit orientation of later spectra covered only the transient (2026 April 23), and edges of the host galaxy light profile (2026 May 13), and were less impacted by atmospheric differential refraction. The sequences on 2026 March 27 and 2026 May 13 were only partially obtained due changing weather conditions. The data were reduced and analyzed using the `DRAGONS` software (K. Labrie et al. 2019).

3. Results and Analysis

3.1. Multiwavelength Lightcurve Modeling

3.1.1. Model Setup

We performed a simultaneous multiwavelength OIR fit to the lightcurve of GRB 260310A in the *grizJK*$_s$ filters using models supplied in the `redback` software package (N. Sarin et al. 2024). Posterior sampling was performed with `Bilby` (G. Ashton et al. 2019) using the nested sampler `dynesty` (J. S. Speagle 2020). We empirically modeled the lightcurve with the combination of a afterglow component plus the contribution of an SN.

For the SN we applied two models. The first was a `redback` model based on the SN 1998bw (T. J. Galama et al. 1998; J. Sollerman et al. 2000, 2002; R. A. Stathakis et al. 2000; F. Patat et al. 2001; A. Clocchiatti et al. 2011), with an extrapolation to extend the wavelength range of the SN's

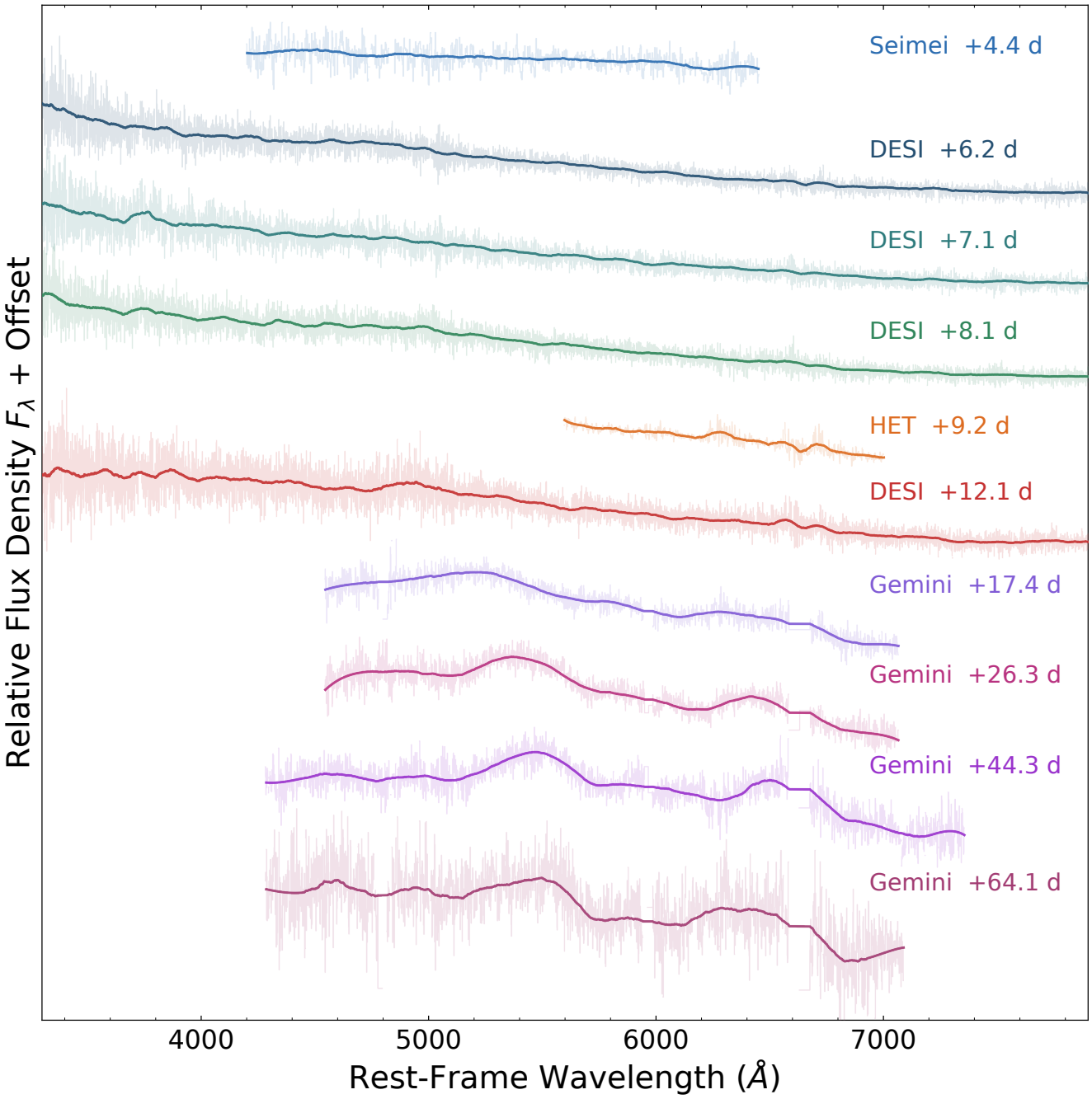


Figure 4. Spectral sequence of GRB 260310A obtained with Seimei, DESI, HET, and Gemini. The spectra are smoothed with a Savitzky–Golay filter (thick lines) and the unsmoothed spectra (thin lines) are also shown. Emission lines and telluric absorption regions have been clipped from the spectra prior to smoothing. The spectra are initially well described by a power law $F_\nu \propto \nu^{-\beta}$ with spectral index $\beta \approx 1.0$ and later evolve to show broad absorption features at ∼5000 and ∼6100 Å.

blackbody spectrum to redder wavelengths to allow joint fitting of the NIR (JK_s) data. Due to this model extrapolation, the JK_s model is less certain and prone to larger uncertainties. The `redback` model is based on the `sncosmo` (K. Barbary et al. 2016) `v19-1998bw` template (M. Vincenzi et al. 2019). This model is parameterized by a simple multiplicative scale factor $k_{98\mathrm{bw}}$ to correct the flux of the template to match observations. A value of $k_{98\mathrm{bw}} = 1$ matches the observed flux scale of SN 1998bw with rest-frame absolute magnitudes $M_B = -18.9$ and $M_V = -19.3$ mag (T. J. Galama et al. 1998). A second fit instead employed a simple Arnett model (W. D. Arnett 1982). This model is parameterized by the nickel fraction f_{Ni}, ejecta mass M_{ej}, ejecta velocity v_{ej}, and floor temperature T_{floor}. In both cases, the models were integrated through the $grizJK_s$ filters using `sncosmo` (K. Barbary et al. 2016) to ensure proper k-corrections were employed to match the observed wavelengths at redshift $z = 0.153$.

The afterglow component was phenomenologically parameterized as a simple temporal broken power law of the form (K. Beuermann et al. 1999; J. E. Rhoads & A. S. Fruchter 2001)

$$F_{\nu,\mathrm{AG}} \propto \nu^{-\beta}\left[\frac{1}{2}\left(\left(\frac{t}{t_{\mathrm{break}}}\right)^{s\alpha_1} + \left(\frac{t}{t_{\mathrm{break}}}\right)^{s\alpha_2}\right)\right]^{-1/s}, \quad (1)$$

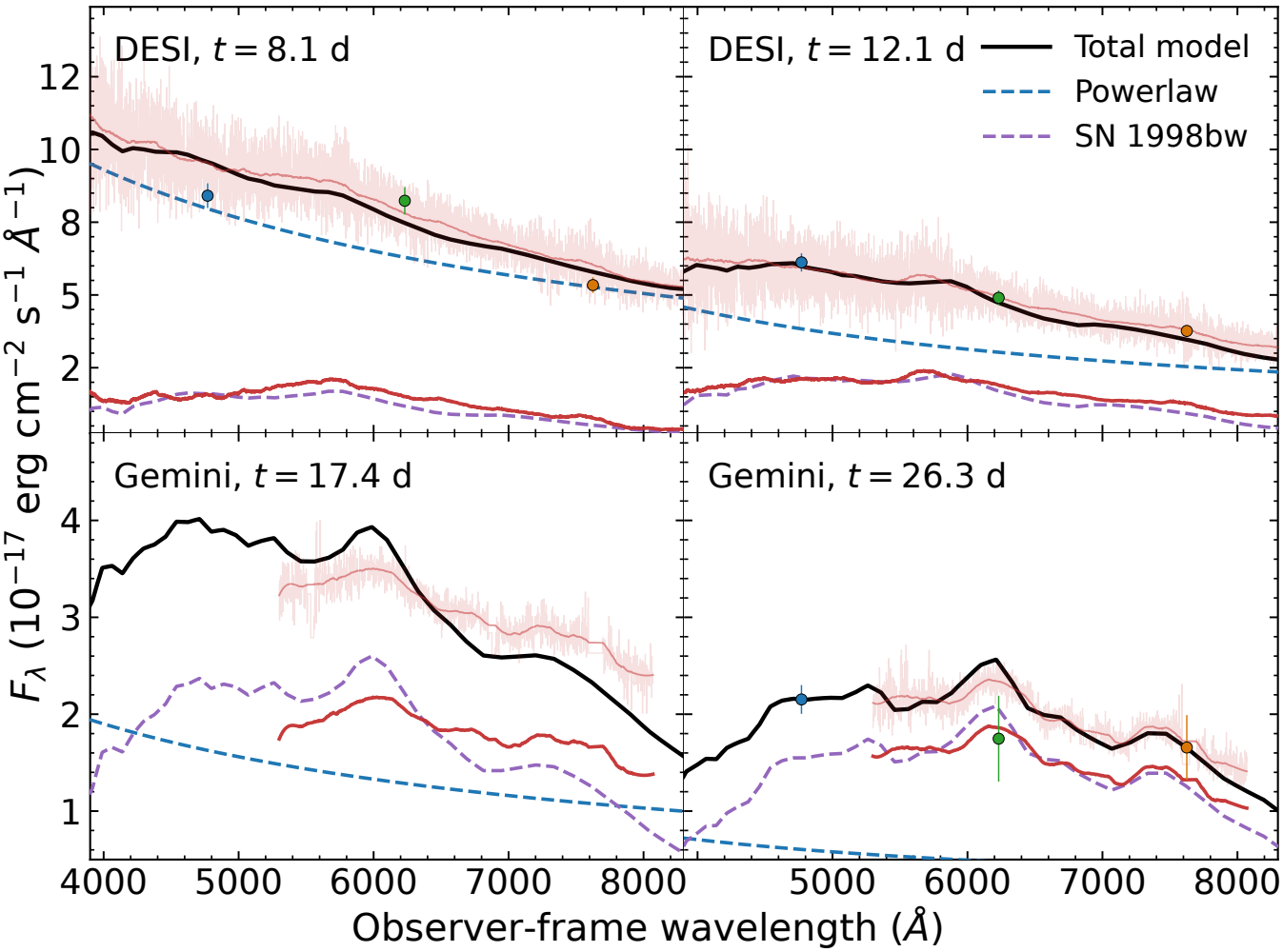


Figure 5. Comparison between the best-fit model derived only from the photometry to the observed DESI and Gemini spectra at 8.1, 12.1, 17.4, and 26.3 days showing the onset and evolution of SN features. The solid black line represents the total model (power law + SN 1998bw) while the blue dashed line represents the power-law component ($F_\nu \propto \nu^{-\beta}$) and the dashed purple line represents the spectral series of SN 1998bw with a flux scaling factor $k_{98bw} = 0.50$. In each panel the observed spectrum is shown both in raw form and smoothed. The thick solid red line represents the smoothed observed spectrum with the power-law component subtracted. The marker color reflects the bandpass of the photometry using the same color scheme as in Figure 3.

where β is the spectral slope of the afterglow, s is the smoothing parameter, and α_1 and α_2 are, respectively, the temporal slopes before and after the break time $t_{\rm break}$. We jointly fit the X-ray lightcurve out to 18.5 days (Y.-H. Yang et al. 2026) in order to constrain the spectral index and postbreak temporal slope, excluding the rebrightening phase (see Section 3.1.2, for further discussion). This fit is shown in Figure 2.

We performed both sets of fits (power law + SN 1998bw and power law + Arnett), which are displayed in Figures 3 and 11 in Appendix B. Both fits were performed with an additional 10% systematic error added in quadrature to the statistical error of each data point to account for uncertainties (e.g., different filter transmission curves) between the different telescopes used.

3.1.2. Comparison of X-Ray and Optical–Near-infrared Behavior

The OIR lightcurve is well described by an initial shallowly decaying power law ($\approx t^{-0.65 \pm 0.07}$) with a temporal break to a steeper decay at ∼8–10 days (observer frame) after the GRB trigger. The postbreak K_s lightcurve shows a steeper decay ($\approx t^{-2.00 \pm 0.15}$) than the optical data ($\approx t^{-1.65 \pm 0.10}$ in g and $\approx t^{-1.47 \pm 0.10}$ in z and J). We show this in Figure 2, where the flux density in the *griK* bands is shown normalized to the flux at the break. This shows clearly the different postbreak slopes in each band.

A similar behavior is also observed at X-rays (R. Jayaraman et al. 2026c), where an initial shallow slope ($\approx t^{-0.35 \pm 0.08}$) breaks to a steeper decay ($\approx t^{-2.05 \pm 0.15}$) after ∼8–10 days (Y.-H. Yang et al. 2026). Thus, we find that the postbreak X-ray decay slope matches the K_s-band slope. The different postbreak decay slopes of the OIR bands can be explained by the contribution of an SN to the optical lightcurve, which serves to flatten out the power-law decay prior to taking over nearly completely at late times. Instead, the K_s band matches the X-ray decline as the SN contributes least to the NIR at that stage of its evolution. This signals that the prebreak lightcurve is dominated instead by the afterglow, as expected. While it is difficult to reconcile the initially shallow decay slopes with standard afterglow closure relations (R. Sari et al. 1998; R. A. M. J. Wijers & T. J. Galama 1999), the achromatic break can be interpreted as a jet break (P. Mészáros & M. J. Rees 1999; J. E. Rhoads 1999; R. Sari et al. 1999; J. Granot & R. Sari 2002).

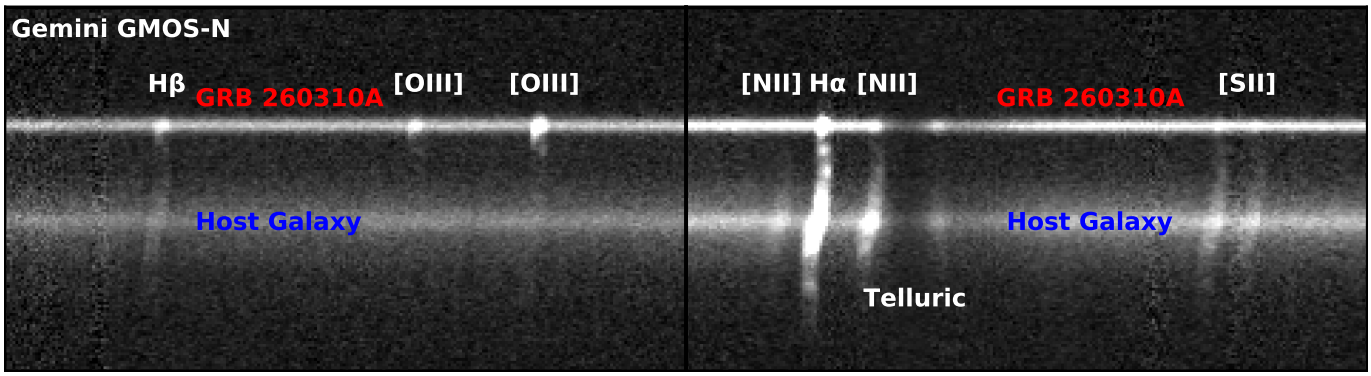


Figure 6. Visualization of the two-dimensional Gemini GMOS-N spectrum obtained on 2026 April 5 (T_0 + 26.3 days). The spectrum covers both the host galaxy (bottom trace) and transient (top trace), as shown in Figure 1. The spectral direction is the *x*-axis, which goes from blue to red wavelengths from left to right. The spatial direction along the slit is the *y*-axis. Each panel covers 300 Å (observer frame) in width and is 11″ in height. The scale is chosen to maximize the visibility of the emission lines. An atmospheric telluric absorption region (the *A* band) is visible to the right of [N II].

Following the achromatic break observed in the X-ray and OIR data, the X-ray lightcurve subsequently exhibited an extremely late-phase plateau (or a rebrightening; R. Gill et al. 2026; K.-R. Hinds et al. 2026b; R. Jayaraman et al. 2026a; G. Waratkar et al. 2026; Y.-H. Yang et al. 2026). The exact origin of the late-time X-ray emission is unclear, though it could be potentially explained by an off-axis jet (J. Granot et al. 2002; E. Rossi et al. 2002; P. Kumar & J. Granot 2003; A. Panaitescu & P. Kumar 2003), a two-component jet (H. Pedersen et al. 1998; E. Berger et al. 2003; K. Sheth et al. 2003; F. Peng et al. 2005), energy injection (B. Zhang & P. Mészáros 2001; E. W. Liang et al. 2006; B. Zhang et al. 2006), refreshed shocks (M. J. Rees & P. Mészáros 1998; P. Kumar & A. Panaitescu 2000; R. Sari & P. Mészáros 2000), inverse-Compton (IC) scattering of optical SN photons (R. A. Chevalier 1982; C.-I. Björnsson & C. Fransson 2004; R. A. Chevalier & C. Fransson 2006; R. Margutti et al. 2012; A. M. Soderberg et al. 2012), or a long-lived magnetar central engine (E. Troja et al. 2007; N. Lyons et al. 2010; A. Rowlinson et al. 2010). We note that additional physics beyond the standard forward shock afterglow are also potentially required to match the shallow X-ray and OIR slopes at early times (see C. T. Christy et al. 2026; R. Gill et al. 2026; Y.-H. Yang et al. 2026).

As the nature of this additional X-ray emission is not certain, it is difficult to predict its impact on the OIR lightcurve, as depending on the interpretation, this rebrightening may or may not contribute to the OIR emission (e.g., IC SN emission would not contribute to the OIR) at late times and with varying contributions. We leave a full analysis of the multiwavelength dataset to future work (see also Y.-H. Yang et al. 2026).

While the timescales of the X-ray rebrightening matches the typical timescales of a Type Ic-BL SN, it is difficult to produce such luminous late-time X-ray emission with IC scattering alone, see, e.g., R. Margutti et al. (2013). If instead the rebrightening impacts the entire broadband afterglow, it could contribute significantly to the OIR depending on the spectral index and spectral energy distribution (SED; e.g., a spectral break between the nonthermal X-ray and OIR emission at late times). We find that while the nonthermal rebrightening is capable of matching the overall OIR brightness, it cannot explain either the (i) SN spectral features out to 40–60 days or (ii) the long-term OIR color evolution (in particular relative to *g* band; see Figure 2). These features strongly suggest a nonthermal rebrightening cannot be the dominant contribution to the observed OIR emission after 20 days. If the rebrightening does contribute at OIR wavelengths then our inferred SN contribution should be taken as an upper limit, though the existence of SN spectral features (see Section 3.2) does require a significant SN component ($k_{98bw} \gtrsim 0.2$) to exist between 20 and 60 days.

If instead the OIR rebrightening at >20 days is due predominantly to the same component as the X-ray rebrightening, and that the OIR and X-ray lie on the same spectral index, this would imply that SN 2026fgk is potentially the faintest GRB-SN observed to date. While this is possible, it is inconsistent with the spectral features of the SN at >40 days, and, according to Occam's razor, it is unlikely to have the faintest GRB-SN also appear in a source exhibiting an extremely odd X-ray rebrightening.

3.1.3. Results of Model Fitting

Our model fits (power law + SN 1998bw and power law + Arnett) are shown in Figures 3 and 11 in Appendix B. The greater flexibility of the simplified Arnett model provides a better match to the SN evolution (Figure 3). While SN 1998bw provides a useful representative case (Figure 11 in Appendix B), the SN evolution of SN 2026fgk is clearly at least slightly different, particularly in the redder bands where it is brighter than SN 1998bw. Additionally, based on our fit, which yields $k_{98bw} \approx 0.4$–0.6, we find that SN 2026fgk is approximately 0.5–1.0 mag fainter than SN 1998bw.

In either case, the exact SN contribution is sensitive to the underlying afterglow contribution (e.g., the late-time temporal index). However, the afterglow decay inferred here agrees well with the X-ray lightcurve out to 18.5 days (Y.-H. Yang et al. 2026). Additionally, our inferred SN ejecta mass of 4–6 $M_\odot$ with nickel mass $\sim$0.4–0.5 $M_\odot$, ejecta velocity of $\sim$16,000 $\pm$ 3000 km s^{-1}, and total kinetic energy $E_k = (3\text{–}8) \times 10^{51}$ erg are in good agreement with other GRB-SN observations (J. Hjorth & J. S. Bloom 2012; Z. Cano 2013; Z. Cano et al. 2017a), see, e.g., Figure 5 of G. P. Srinivasaragavan et al. (2023).

3.2. Spectral Analysis and Supernova Features

We obtained an optical spectral sequence (Figure 4) of GRB 260310A starting at 4.4 days and continuing to 64 days in the observer frame. The timing of our spectral sequence

relative to the lightcurve is shown in Figure 3. The early spectra from Seimei, DESI, and HET are well described by a power law $F_\nu \propto \nu^{-\beta}$ with spectral index $\beta \approx 1.0$. This agrees with the photometry-based SEDs at <8 days and our lightcurve modeling in Section 3.1. This observed spectral index can also be explained by $\beta \approx 0.9$ extincted by a visual extinction $A_V \approx 0.1$ mag from dust intrinsic to the source environment at $z = 0.153$, which provides a better agreement with the X-ray data (Y.-H. Yang et al. 2026).

The spectra clearly evolve and display broad undulations typical of Type Ic-BL SNe at later times. We associate these with blueshifted Fe II λ5169 and Si II λ6355 absorption at high velocities $> 10^4$ km s^{-1}, typical of GRB-SNe. The later spectra obtained with Gemini are noisy and suffer from telluric absorption and chip gaps in critical regions of the Si II absorption features. However, the evolution of the features is clear. In fact, we find evidence for deviations from the power law in spectra obtained at 8.1 and 12.1 days by DESI. These features agree well with the expectations from our power law + SN 1998bw fit to the photometry, which included no additional spectral information. This is shown in Figure 5, which displays the SED of the power law + SN 1998bw fit to the OIR lightcurves (see Section 3.1) at 8.1, 12.1, 17.4, and 26.3 days versus the relevant DESI and Gemini spectra. We show the total model and the individual components. Additionally, we have subtracted the power-law component from the observed spectra after smoothing. This shows good agreement with the features and evolution of SN 1998bw. The spectra suggest that the velocity of the Fe II feature was initially faster than SN 1998bw at 8.1 and 12.1 days, but slowed down by 17.4 and 26.3 days to below the speed of SN 1998bw's ejecta. While this is not an exact template match to the observed spectra, it provides a useful diagnostic and comparison to the canonical GRB-SN. This comparison, and the observed spectra, provide conclusive evidence than GRB 260310A was associated with a standard collapsar progenitor that produced a Type Ic-BL GRB-SN. Additionally, the SN features definitively show that the optical rebrightening has to have a significant, likely dominant, SN contribution.

The SN features continue to be clearly seen out to late times. Figure 4 shows the presence of the bumpy SN spectra at 44.3 and 64.1 days. We note that the final Gemini spectrum at 64.1 days is noisier due to a combination of fading of the source and that only one-half the planned sequence was executed due to changing weather conditions. However, despite this, the bump at 5500 Å is still clearly visible. Between 44.3 and 64.1 days the Fe II λ5169 features gradually declined, as observed for other nearby Type Ic-BL SNe at similar distances (see, e.g., J. C. Rastinejad et al. 2025; G. P. Srinivasaragavan et al. 2025a, 2025b).

3.3. Environmental Analysis of Gamma-Ray Burst Site and Galaxy

GRB 260310A is located at a large angular offset of $5''.4 \pm 0''.2$ from its host galaxy (Figure 1). We obtained Gemini spectra (Table 2) that covered both the transient and host galaxy with the slit aligned as shown in Figure 1. A visualization of the two-dimensional spectra is shown in Figure 6 that clearly demonstrates that the GRB explosion site and nearby galaxy are located at $z = 0.1530$ and 0.1525, respectively, with only a small velocity offset of $\sim$100 km s^{-1} between them, likely due to the galaxy's rotation. This velocity offset, as well as the rotation curve of the galaxy, are visible in Figure 6. At this redshift, the projected physical offset between the galaxy's centroid and the GRB explosion site is 14.8 ± 0.6 kpc. Figure 6 shows a "bridge" of star formation reaching from the galaxy to the GRB site along the slit. The next closest knot of star formation observed along the slit is 1.3 kpc from the GRB's explosion site. Tracing the galaxy rotation curve of Hα back along the slit, we find that even in the opposite direction the ongoing star formation in the galaxy's disk extends to at least $6''$ from the center of the galaxy. This is consistent with the offset of the GRB, and shows that its observed location fits within the light profile of the galaxy, as traced by ongoing star formation. Additionally, deep imaging ($g > 25$ AB mag) obtained with FTW/3KK at later times clearly shows the morphology of the galaxy is that of a central bulge superimposed on a disk that extends to the GRB explosion site.

We performed an analysis of the nebular emission lines of both the GRB site and host galaxy to explore their individual properties. The GRB explosion site shows common nebular emission lines associated with ongoing star formation (Figure 6), including the [O II] doublet at $\lambda\lambda$3726, 3729, nebular [O III] at $\lambda\lambda$4959, 5007, Balmer lines (Hα, Hβ, Hγ, Hδ, Hϵ, and Hζ), [Ne III] at λ3869, He I λ5876, and the [N II] and [S II] doublets. The host galaxy shows weaker emission features and deep Balmer and calcium absorption that together indicate both an old stellar population and a new burst of star formation. For the host, Hβ is detected in both emission and absorption with a slight velocity shift in the centroid of those components. This may be due to the rotation curve of the galaxy, but likely also shows that the kinematics (and locations) of the old and new stellar populations in the host galaxy are different. We also detect Na I D absorption from the host galaxy, but not at the location of the transient.

We used the penalized pixel-fitting (pPXF) software (M. Cappellari & E. Emsellem 2004; M. Cappellari 2012, 2017) to fit the optical spectra and derive the relevant emission line fluxes. We utilized the E-MILES stellar library (A. Vazdekis et al. 2016). At the transient location, we derive a near–Case B recombination Balmer decrement $H\alpha/H\beta = 2.76 \pm 0.12$ (D. E. Osterbrock 1989); Baldwin–Phillips–Terlevich (BPT; J. A. Baldwin et al. 1981) ratios of $\log([O\,III]/H\beta) = 0.46 \pm 0.02$ and $N2 \equiv \log([N\,II]/H\alpha) = -0.95 \pm 0.03$ placing the transient location firmly in the star-forming region; and a subsolar gas phase metallicity $12 + \log(O/H) \approx 8.2-8.3$ (roughly $0.4\,Z_\odot$) derived from N2 and O3N2 (M. Pettini & B. E. J. Pagel 2004; R. A. Marino et al. 2013), where we adopt a solar metallicity of $12 + \log(O/H) = 8.69$ (M. Asplund et al. 2004, 2009). The statistical uncertainty ($\sim\pm0.05$) on the metallicity is smaller than the systematic uncertainty (0.1–0.2 dex) on the calibration (M. Pettini & B. E. J. Pagel 2004; R. A. Marino et al. 2013). From the Hα luminosity at the transient location, we derive a star formation rate (SFR) of $0.85 \pm 0.10\,M_\odot$ yr^{-1} (R. C. J. Kennicutt 1998) using a Chabrier (G. Chabrier 2003) initial mass function.

For the host galaxy, we derived $\log([N\,II]/H\alpha) = -0.34 \pm 0.01$ and $\log([O\,III]/H\beta) = -0.44 \pm 0.05$. From these, we obtain a near-solar metallicity of $12 + \log(O/H) \approx 8.6$–8.7 from O3N2 and N2 (M. Pettini & B. E. J. Pagel 2004; R. A. Marino et al. 2013). Therefore, the host galaxy has a higher metallicity than the GRB explosion site. While these quoted errors do not include the

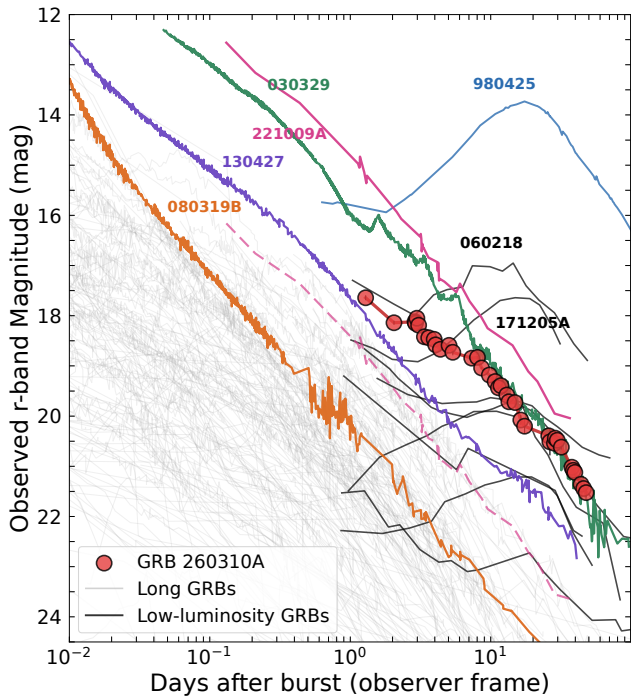


Figure 7. Observed optical lightcurves of long GRBs (gray) and low-luminosity GRBs (black) compared to GRB 260310A (red circles). A few specific GRBs are highlighted for a more specific comparison. GRB 221009A (magenta) is shown both observed (dashed) and dust corrected (solid). Data have been compiled from T. J. Galama et al. (1998), E. H. McKenzie & B. E. Schaefer (1999), J. Sollerman et al. (2000, 2002, 2006), E. Pian et al. (2006), D. A. Kann et al. (2006, 2010, 2011), A. Clocchiatti et al. (2011), A. Nicuesa Guelbenzu et al. (2012), D. A. Perley et al. (2014), V. D'Elia et al. (2018), and B. O'Connor et al. (2023).

intrinsic calibration scatter, which is of order ∼0.18 dex for O3N2 and ∼0.16 dex for N2 from R. A. Marino et al. (2013), both diagnostics show the same trend that the GRB environment has a lower metallicity by roughly 0.3–0.5 dex. In the context of the comparison sample shown in Figure 10, the local GRB site sits in the region more commonly occupied by resolved GRB explosion sites compared to the integrated host value.

4. Discussion

4.1. Optical Afterglow Properties

Due to its nearby distance ($z = 0.153$), GRB 260310A displays an extremely bright multiwavelength counterpart. At optical wavelengths, it is among the brightest GRB afterglows ever discovered. To demonstrate this, in Figure 7, we show the *r*-band lightcurve of GRB 260310A versus a sample of 190 long GRB afterglows. The optical lightcurves shown in Figure 7 were largely obtained from a public repository[17] of GRB lightcurves initially compiled by D. A. Kann (see D. A. Kann et al. 2006, 2010, 2011; A. Nicuesa Guelbenzu et al. 2012) and supplemented by additional events.

Based on this, we find that GRB 260310A displays the brightest observed optical afterglow in the era of the Neil Gehrels Swift Observatory (N. Gehrels et al. 2004) at optical wavelengths (see also R. Gill et al. 2026; K.-R. Hinds et al. 2026b; Y.-H. Yang et al. 2026). This is largely due to the intervening Galactic dust impacting GRB 221009A (T. Laskar et al. 2023; A. J. Levan et al. 2023; B. O'Connor et al. 2023), as its dust-corrected brightness exceeds GRB 260310A. Additionally, we have excluded GRB 980425, GRB 060218, and GRB 171205A, see Figure 7. While these bursts clearly exceed its brightness at optical wavelengths, their optical lightcurves are generally attributed to a combination of shock cooling emission at early times and SN emission at late times (e.g., S. Campana et al. 2006; E. Pian et al. 2006; A. M. Soderberg et al. 2006; Z. Cano et al. 2011; L. Izzo et al. 2019). They simply exceed the observed brightness of GRB 260310A due to their significantly closer distances. Comparing GRB 260310A to energetic GRBs at a similar redshift ($z \approx 0.15$), such as GRB 221009A at $z = 0.151$ (A. de Ugarte Postigo et al. 2022; D. B. Malesani et al. 2025) and GRB 030329 at $z = 0.1685$ (J. Hjorth et al. 2003; K. Z. Stanek et al. 2003), we find that it closely matches the observed brightness of GRB 030329, while lying below the dust-corrected lightcurve of GRB 221009A.

However, even correcting for the redshift, we find that GRB 260310A is among the most luminous GRB afterglows, and comparable to GRB 130427A ($z = 0.34$; D. Xu et al. 2013; A. Maselli et al. 2014; D. A. Perley et al. 2014; W. T. Vestrand et al. 2014) and GRB 030329 at late times ($\gtrsim$10 days). At this phase the SN contribution begins to emerge (Figure 3) and takes over as the primary contributor to the lightcurve.

4.2. Comparison to Other Gamma-Ray Burst Supernovae

Here we compare the properties of GRB 260310A/SN 2026fgk to other Type Ic-BL GRB-SNe identified in the literature. We compiled and cross checked the nearby GRB-SN sample by combining multiple GRB-SN catalogs (J. Hjorth & J. S. Bloom 2012; Z. Cano et al. 2017a; G. Finneran et al. 2025) and adding more recent secure additions to the literature (e.g., S. Klose et al. 2019). In total, there are 73 GRB-SNe that have been identified in the literature (see, e.g., G. Finneran et al. 2025, and references therein), of which 38 have spectroscopic classifications of varying signal-to-noise ratio depending largely on the burst's redshift and afterglow brightness. Within $z < 0.2$, there are 11 previous GRB-SNe, making GRB 260310A the twelfth case of a low-z GRB-SN with spectroscopic confirmation. These events are GRB 980425/SN 1998bw (T. J. Galama et al. 1998; R. A. Stathakis et al. 2000; F. Patat et al. 2001), GRB 030329/SN 2003dh (J. Hjorth et al. 2003; T. Matheson et al. 2003; K. Z. Stanek et al. 2003), GRB 031203/SN 2003lw (D. Malesani et al. 2004), GRB 060218/SN 2006aj (S. Campana et al. 2006; P. Ferrero et al. 2006; P. A. Mazzali et al. 2006; E. Pian et al. 2006; A. M. Soderberg et al. 2006; J. Sollerman et al. 2006), GRB 100316D/SN 2010bh (R. Chornock et al. 2010; Z. Cano et al. 2011; Y.-Z. Fan et al. 2011; R. L. C. Starling et al. 2011; F. Bufano et al. 2012; E. F. Olivares et al. 2012), GRB 130702A/SN 2013dx (V. D'Elia et al. 2015; V. L. Toy et al. 2016; A. A. Volnova et al. 2017; P. A. Mazzali et al. 2021), GRB 161219B/SN 2016jca (Z. Cano et al. 2017b; C. Ashall et al. 2019), GRB 171205A/SN 2017iuk (V. D'Elia et al. 2018; J. Wang et al. 2018; L. Izzo et al. 2019), GRB 180728A/SN 2018fip (A. Rossi et al. 2026), GRB 190829A/SN 2019oyw (Y.-D. Hu et al. 2021; K. Bhirombhakdi et al. 2024), and GRB 221009A/SN 2022xiw (M. D. Fulton et al. 2023; M. Shrestha et al. 2023; G. P. Srinivasaragavan et al. 2023; P. K. Blanchard et al. 2024). Since the launch of the Einstein Probe (EP; W. Yuan et al. 2025), there

[17] https://github.com/steveschulze/kann_optical_afterglows

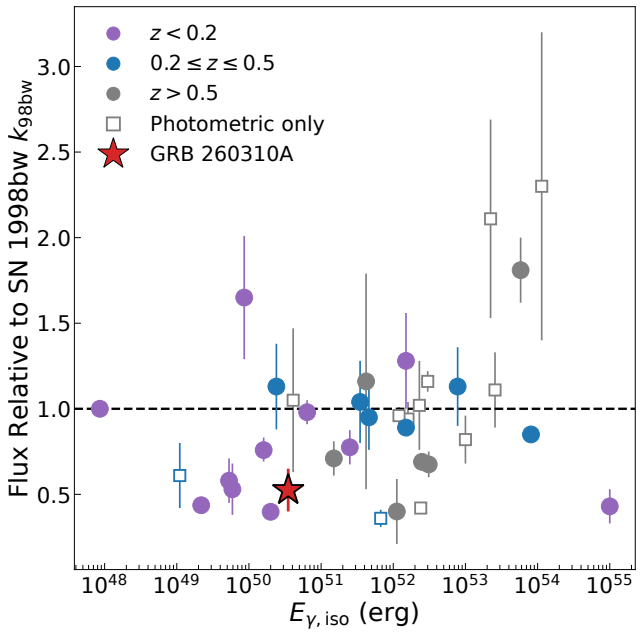


Figure 8. The flux-stretching factor k_{98bw} relative to SN 1998bw in rest-frame V band of a sample of GRB-SNe is shown vs. the isotropic-equivalent gamma-ray energy $E_{\gamma,\mathrm{iso}}$ release of the GRB prompt emission. The data were compiled from J. Hjorth & J. S. Bloom (2012), J. Hjorth (2013), J. Greiner et al. (2015), Z. Cano et al. (2017a, 2017b), S. Klose et al. (2019), L. Izzo et al. (2019), Y.-D. Hu et al. (2021), G. P. Srinivasaragavan et al. (2023), Y.-D. Hu et al. (2021), A. Rossi et al. (2026), and references therein. This figure is reproduced from J. Hjorth (2013) and G. P. Srinivasaragavan et al. (2023).

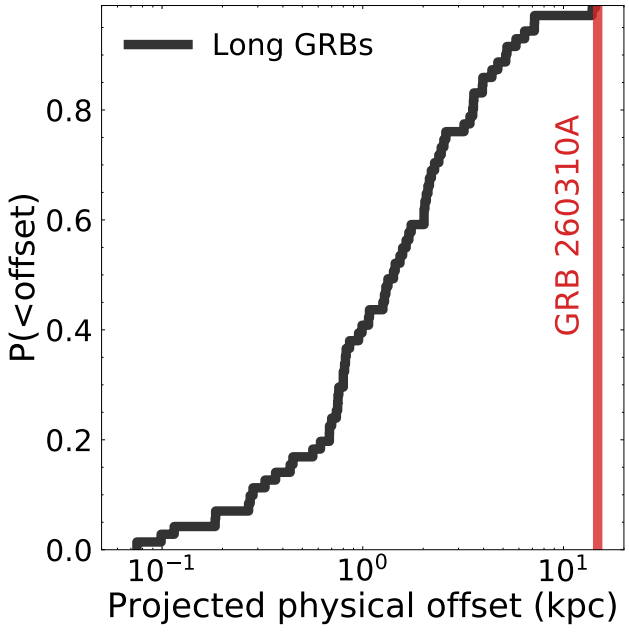


Figure 9. Cumulative distribution of projected physical offsets for long GRBs from their host galaxies (P. K. Blanchard et al. 2016; J. D. Lyman et al. 2017). The location of GRB 260310A is shown as a red vertical line.

have been an additional four Type Ic-BL SNe associated with high-energy (X-ray) detections at $z < 0.2$: EP250108a/SN 2025kg (R. A. J. Eyles-Ferris et al. 2025; J. C. Rastinejad et al. 2025; G. P. Srinivasaragavan et al. 2025a; W. X. Li et al. 2025), EP250304A/SN 2025fhm (L. Izzo et al. 2025; L. Cotter et al. 2026), EP250827b/SN 2025wkm (G. P. Srinivasaragavan et al. 2025b), and, occurring after the discovery of GRB 260310A, EP260321a/SN 2026gzf (T.-W. Chen et al. 2026; G. Corcoran et al. 2026; A. Martin-Carrillo et al. 2026c; B. O'Connor et al. 2026a; J. C. Rastinejad et al. 2026; W. Yuan et al. 2026).

In Figure 8, we compare the flux-stretching factor k_{98bw} of these GRB-SNe relative to the canonical SN 1998bw (T. J. Galama et al. 1998) versus the isotropic-equivalent gamma-ray energy release of the GRB's prompt emission. While it is well known that there is no significant correlation between the SN brightness and the GRB prompt emission (e.g., J. Hjorth 2013; S. Schulze et al. 2014; G. P. Srinivasaragavan et al. 2023), there is an obvious selection effect of identifying the faintest explosions, of both types, at low redshifts ($z < 0.2$). We find that GRB 260310A matches well with the distribution of other GRB-SNe (see also R. Gill et al. 2026; K.-R. Hinds et al. 2026b).

Additionally, our inferred SN ejecta mass of 4–6 $M_\odot$ with nickel mass ~ 0.4–$0.5\,M_\odot$ and total kinetic energy $E_k = (3\text{–}8) \times 10^{51}$ erg align well with other GRB-SNe. For example, the analysis of Z. Cano et al. (2017a) presents "average" GRB-SN properties of $E_k = (2.5 \pm 1.8) \times 10^{52}$ erg, $M_{ej} = 6 \pm 4\,M_\odot$, and $M_{Ni} = 0.4 \pm 0.2\,M_\odot$. These are consistent with the agreement between the SN 1998bw flux-stretching inferred for SN 2026fgk as compared to other GRB-SNe (see Figure 8).

4.3. Local Environment and Galactocentric Offset

Long GRBs are understood to arise from the deaths of massive stars (S. E. Woosley 1993; S. E. Woosley & J. S. Bloom 2006) and are therefore expected to trace recent star formation. Consistent with that picture, population studies have shown that long GRBs are typically concentrated on the brightest ultraviolet light of their hosts at small galactocentric offsets (J. S. Bloom et al. 2002; A. S. Fruchter et al. 2006; P. K. Blanchard et al. 2016; J. D. Lyman et al. 2017). GRB 260310A is unusual in this context because its projected separation from its host galaxy is large, $5\farcs4 \pm 0\farcs2$, corresponding to a projected physical offset of 14.8 ± 0.6 kpc at $z = 0.1530$ (Figure 1). This is 10× larger than the median value for long GRBs (P. K. Blanchard et al. 2016; see Figure 9). However, the host normalized offset is only $R/R_e = 2.3 \pm 0.1$, where $R_e = 2\farcs4$ is the half-light radius of the host galaxy. Moreover, the Gemini spectra demonstrate that the burst is not dynamically detached from the host (Figure 6). Instead, the redshift difference between the GRB site ($z = 0.153$) and the host ($z = 0.1525$) is only ~ 100 km s^{-1}; nebular emission forms a clear bridge between the galaxy and the burst position; and Hα emission extends to comparable distances on the opposite side of the galaxy (Figure 6). Taken together, these observations indicate that GRB 260310A occurred in an outlying H II region embedded within an extended, low surface brightness star-forming disk, rather than in an isolated satellite or halo environment. In that sense, the event appears to belong to the same broader class of long GRBs with large galactocentric offsets (>5 kpc) but still clearly locally star-forming environments identified in other low-redshift systems (L. Christensen et al. 2008; E. M. Levesque et al. 2011; S. Schulze et al. 2014; L. Izzo et al. 2017; A. Melandri et al. 2019; C. C. Thöne et al. 2024).

The GRB site itself remains actively star forming, with $\mathrm{SFR}_H\alpha \approx 1\,M_\odot\,\mathrm{yr}^{-1}$, and is clearly less metal enriched than the host galaxy ($12 + \log(\mathrm{O/H}) \approx 8.6$), with a subsolar metallicity $12 + \log(\mathrm{O/H}) \approx 8.3$ (see Section 3.3). This is consistent with the expectations for a collapsar progenitor and with observations of other GRB environments (e.g.,

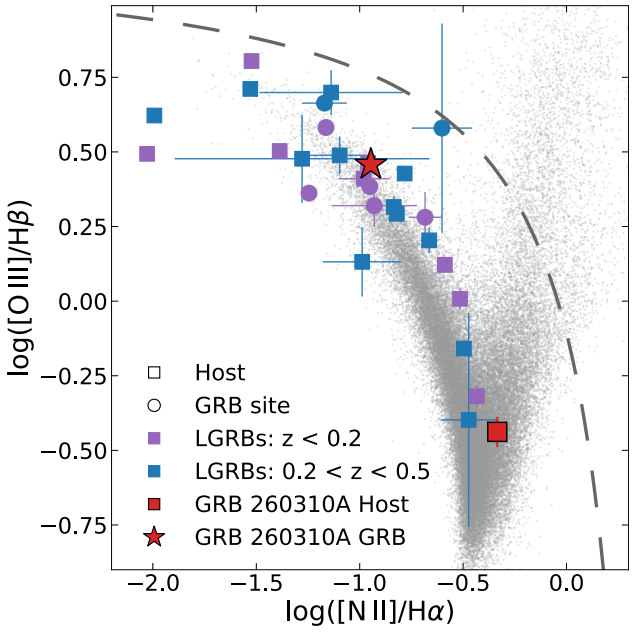


Figure 10. BPT diagram for long GRB host galaxies (squares) and explosion sites (circles) compared to a background population of Sloan Digital Sky Survey galaxies (small gray circles; D. G. York et al. 2000; H. Aihara et al. 2011; V. Stampoulis et al. 2019). Both the explosion site (red star) and integrated host galaxy (red square) of GRB 260310A are shown. The long GRB data are compiled from L. Christensen et al. (2008), X. H. Han et al. (2010), P. L. Kelly et al. (2013), S. Schulze et al. (2014), E. R. Stanway et al. (2015), T. Krühler et al. (2015), L. Izzo et al. (2017), Z. Cano et al. (2017b), K. E. Heintz et al. (2018), A. de Ugarte Postigo et al. (2018, 2020), A. Melandri et al. (2019), and C. C. Thöne et al. (2024).

E. M. Levesque et al. 2010a, 2010b; T. Krühler et al. 2015). Thus, while the burst occurred at large projected radius, it has a locally favorable environment for long GRB production, namely a star-forming region with lower metallicity than the galaxy-integrated value (Figure 10). That result is fully consistent with the resolved view of nearby long GRB hosts, in which the immediate burst environment is often less enriched than the host as a whole even when the galaxy-integrated spectrum appears comparatively evolved (E. M. Levesque et al. 2011; C. C. Thöne et al. 2014; T. Krühler et al. 2015, 2017; Z. Cano et al. 2017b; L. Izzo et al. 2017; M. J. MichałowskI et al. 2018; M. Tanga et al. 2018; A. Melandri et al. 2019; C. C. Thöne et al. 2021, 2024). GRB 260310A therefore illustrates an important point about the interpretation of GRB host environments. Large projected offsets do not necessarily imply that the progenitor formed in a remote or quiescent region of the host galaxy. In this case, our Gemini spectroscopy definitively shows that the burst site is part of a continuous star-forming structure connected to the main body of the galaxy, and that the metallicity declines toward that outer region approaching the GRB explosion site (Figure 6).

5. Conclusions

We present the results of our comprehensive OIR observing campaign of GRB 260310A utilizing FTW, Seimei, DESI, HET, and Gemini. At the nearby distance of $z = 0.153$ (756 Mpc), GRB 260310A provided a critical opportunity to search for and identify an SN component. Our investigation yielded the spectroscopic classification of the associated SN 2026fgk, confirming GRB 260310A's relation to other long GRBs with collapsar progenitors. SN 2026fgk is only the twelfth GRB-SN uncovered within 1 Gpc ($z < 0.2$) since 1998. It is the fifteenth Type Ic-BL SN within 1 Gpc associated with a prompt high-energy transient when including recent EP fast X-ray transients and adds to the growing sample of spectroscopically classified GRB-SNe.

We find that the optical afterglow of GRB 260310A is among the brightest ever observed, matching GRB 030329 at late times and exceeding the observed optical lightcurve of GRB 221009A. The brightness of the afterglow, combined with the rather smooth onset of SN features, masked the SN discovery and it was not robustly uncovered spectrally until ∼17 days posttrigger. Only a handful of $z < 0.2$ GRB-SNe had SN spectral features identified later than this, e.g., GRB 031203/SN 2003lw (D. Malesani et al. 2004) and GRB 221009A/SN 2022xiw (P. K. Blanchard et al. 2024).

Additionally, while the ∼15 kpc offset of GRB 260310A from its putative host galaxy is among the largest ever observed for a long GRB, we find that this is simply due to an offset H II region. This H II region is linked to the host galaxy by a bridge of star formation as observed along the Gemini GMOS slit. The offset is in the direction of the extension of the host galaxy disk, and we find that it is simply due to an extended low surface brightness disk. The GRB explosion site has a very low metallicity compared to the host galaxy, as expected for a collapsar progenitor and consistent with the explosion sites of other GRB-SNe.

GRB 260310A continues the line of low-redshift ($z < 0.2$) GRBs with outlier properties in both prompt emission and galactocentric offset, and demonstrates the diversity in GRB explosion properties. Due to its nearby distance and circumpolar sky position, additional observations of both the GRB-SN and afterglow to significantly later times are both possible and warranted to improve constraints on the physical parameters of the explosion. We strongly encourage additional follow-up at all wavelengths.

Acknowledgments

The authors thank the referee for providing useful comments and suggestions.

B.O. thanks the Gemini Director Time Review Board (GDTRB), including Aleksandar Cikota, Hwihyun Kim, Bryan Miller, Siyi Xu, and Elena Sabbi, for approving the DDT request. B.O. is grateful for the excellent support of Atsuko Nitta, Teo Mocnik, Jen Andrews, Sunny Stewart, Denise Hung, Kristin Chiboucas, Hyewon Suh, and the entire Gemini-North staff in rapidly scheduling and obtaining these observations.

B.O. is supported by the McWilliams Postdoctoral Fellowship in the McWilliams Center for Cosmology and Astrophysics at Carnegie Mellon University.

This paper contains data obtained at the Wendelstein Observatory of the Ludwig-Maximilians University Munich. Funded by the Deutsche Forschungsgemeinschaft (DFG; German Research Foundation) under Germany's Excellence Strategy–EXC-2094/2–390783311. The authors acknowledge the IT Support Team of the Faculty of Physics at LMU for maintaining and supporting the high-performance computing (HPC), storage, and computational infrastructure used in this work.

This material is based upon work supported by the U.S. Department of Energy (DOE), Office of Science, Office of High-Energy Physics, under Contract No. DE–AC02–05CH11231, and by the National Energy Research Scientific Computing Center, a DOE Office of Science User Facility under the same contract. Additional support for DESI was provided by the U.S. National Science Foundation (NSF), Division of Astronomical Sciences under Contract No. AST-0950945 to the NSF's National Optical-Infrared Astronomy Research Laboratory; the Science and Technology Facilities Council of the United Kingdom; the Gordon and Betty Moore Foundation; the Heising-Simons Foundation; the French Alternative Energies and Atomic Energy Commission (CEA); the National Council of Humanities, Science, and Technology of Mexico (CONAHCYT); the Ministry of Science, Innovation, and Universities of Spain (MICIU/AEI/10.13039/501100011033); and by the DESI Member Institutions: https://www.desi.lbl.gov/collaborating-institutions. The authors are honored to be permitted to conduct scientific research on I'oligam Du'ag (Kitt Peak), a mountain with particular significance to the Tohono O'odham Nation. Any opinions, findings, and conclusions or recommendations expressed in this material are those of the author(s) and do not necessarily reflect the views of the U. S. National Science Foundation, the U. S. Department of Energy, or any of the listed funding agencies.

Based on observations obtained at the international Gemini Observatory, a program of NSF's OIR Lab, which is managed by the Association of Universities for Research in Astronomy (AURA) under a cooperative agreement with the National Science Foundation on behalf of the Gemini Observatory partnership: the National Science Foundation (United States), National Research Council (Canada), Agencia Nacional de Investigación y Desarrollo (Chile), Ministerio de Ciencia, Tecnología e Innovación (Argentina), Ministério da Ciência, Tecnologia, Inovações e Comunicações (Brazil), and Korea Astronomy and Space Science Institute (Republic of Korea). The data were acquired through the Gemini Observatory Archive at NSF NOIRLab and processed using Data Reduction for Astronomy from Gemini Observatory North and South (`DRAGONS`). The authors wish to recognize and acknowledge the very significant cultural role and reverence that the summit of Maunakea has always had within the indigenous Hawaiian community.

This paper contains data from observations obtained with the Hobby-Eberly Telescope (HET), which is a joint project of the University of Texas at Austin, the Pennsylvania State University, Ludwig-Maximillians-Universität München, and Georg-August Universität Göttingen. The HET is named in honor of its principal benefactors, William P. Hobby and Robert E. Eberly. We acknowledge the Texas Advanced Computing Center (TACC) at The University of Texas at Austin for providing high-performance computing, visualization, and storage resources that have contributed to the results reported within this paper. The Low Resolution Spectrograph 2 (LRS2) was developed and funded by the University of Texas at Austin, McDonald Observatory, Department of Astronomy, and Pennsylvania State University. We thank the Leibniz-Institut für Astrophysik Potsdam (AIP) and the Institut für Astrophysik Göttingen (IAG) for their contributions to the construction of the integral-field units.

The authors thank the TriCCS developer team (which has been supported by the JSPS KAKENHI grant Nos. JP18H05223, JP20H00174, and JP20H04736, and by NAOJ Joint Development Research).

This research has made use of the GRBSN webtool (G. Finneran et al. 2025), available at https://grbsn.watchertelescope.ie.

Facilities: WO:2m, Seimei, Gemini:Gillett, Mayall, HET.

Software: `Astropy` (Astropy Collaboration et al. 2013, 2018, 2022), `SFFT` (L. Hu et al. 2022), `AstrOmatic` (E. Bertin & S. Arnouts 1996; E. Bertin 2006, 2010; E. Bertin et al. 2002), `DRAGONS` (K. Labrie et al. 2019, 2023), `pPXF` (M. Cappellari & E. Emsellem 2004; M. Cappellari 2012, 2017), `redback` (N. Sarin et al. 2024), `Bilby` (G. Ashton et al. 2019), `dynesty` (J. S. Speagle 2020), `sncosmo` (K. Barbary et al. 2016).

Appendix A
Log of Observations

In Tables 1 and 2, we present a log of all photometric and spectroscopic observations obtained and analyzed in this work.

Table 1
Log of Photometry of GRB 260310A from FTW and Seimei

Start Time (UT)	ΔT (days)	Exposure (s)	Telescope	Filter	AB Magnitude
2026-03-13 19:37:11	3.61	2160	FTW	g	18.66 ± 0.01
2026-03-13 19:37:11	3.61	2160	FTW	i	18.16 ± 0.01
2026-03-13 19:37:28	3.61	2037	FTW	J	17.50 ± 0.01
2026-03-13 19:48:45	3.62	2400	FTW	r	18.39 ± 0.01
2026-03-13 19:48:45	3.62	1950	FTW	z	17.94 ± 0.02
2026-03-13 19:49:01	3.62	1432	FTW	K_s	17.07 ± 0.01
2026-03-14 14:05:06	4.38	210	Seimei	r	18.62 ± 0.04
2026-03-14 14:05:06	4.38	210	Seimei	g	18.87 ± 0.03
2026-03-14 14:05:06	4.38	90	Seimei	i	18.35 ± 0.04
2026-03-14 14:07:44	4.38	120	Seimei	z	18.11 ± 0.04
...	...	...	...	...	...

Note. Times ΔT are given relative to the GRB trigger. The photometry has been corrected for Galactic reddening $E(B-V) = 0.02$ mag (E. F. Schlafly & D. P. Finkbeiner 2011). The full version of this table is available in machine-readable format in the online journal. A portion is shown here for guidance regarding its form and function.

(This table is available in its entirety in machine-readable form in the online article.)

Table 2
Log of Spectroscopic Observations of GRB 260310A/SN 2026fgk

Start Date (UTC)	ΔT (days)	Telescope	Instrument	Grating	Exposure (s)
2026-03-14 14:24:00	4.39	Seimei	KOOLS-IFU	VPH-Blue	2550
2026-03-15 14:09:36	5.38	Seimei	KOOLS-IFU	VPH-Red	2700
2026-03-16 08:53:08	6.16	Mayall	DESI	⋯	1200
2026-03-17 08:07:32	7.13	Mayall	DESI	⋯	1200
2026-03-18 06:49:15	8.08	Mayall	DESI	⋯	1200
2026-03-19 09:50:00	9.20	HET	LRS2	LRS2-R	1800
2026-03-22 06:59:22	12.08	Mayall	DESI	⋯	1200
2026-03-27 14:56:32	17.42	Gemini-North	GMOS	B480	2120
2026-04-05 12:40:09	26.32	Gemini-North	GMOS	B480	4000
2026-04-20 13:09:59	41.34	Gemini-North	GMOS	B480	5901
2026-04-23 12:02:23	44.30	Gemini-North	GMOS	B480	6000
2026-05-13 07:43:05	64.12	Gemini-North	GMOS	B480	4000

Appendix B
Additional Model Fitting Results

In Figure 11 we show the best-fit model to the multiwavelength lightcurve for the power law + SN 1998bw model with an SN 1998bw flux scaling factor of $k_{98bw} = 0.50$. The use of SN 1998bw as a template is the standard adopted method for such analyses in the literature (e.g., J. S. Bloom et al. 1999; A. Zeh et al. 2004). We note that the NIR (JK_s) behavior of the model is uncertain and due to extrapolation to wavelengths beyond the available templates for SN 1998bw (e.g., `v19-1998bw`; M. Vincenzi et al. 2019). The JK_s model lightcurves of SN 1998bw should therefore be interpreted with caution.

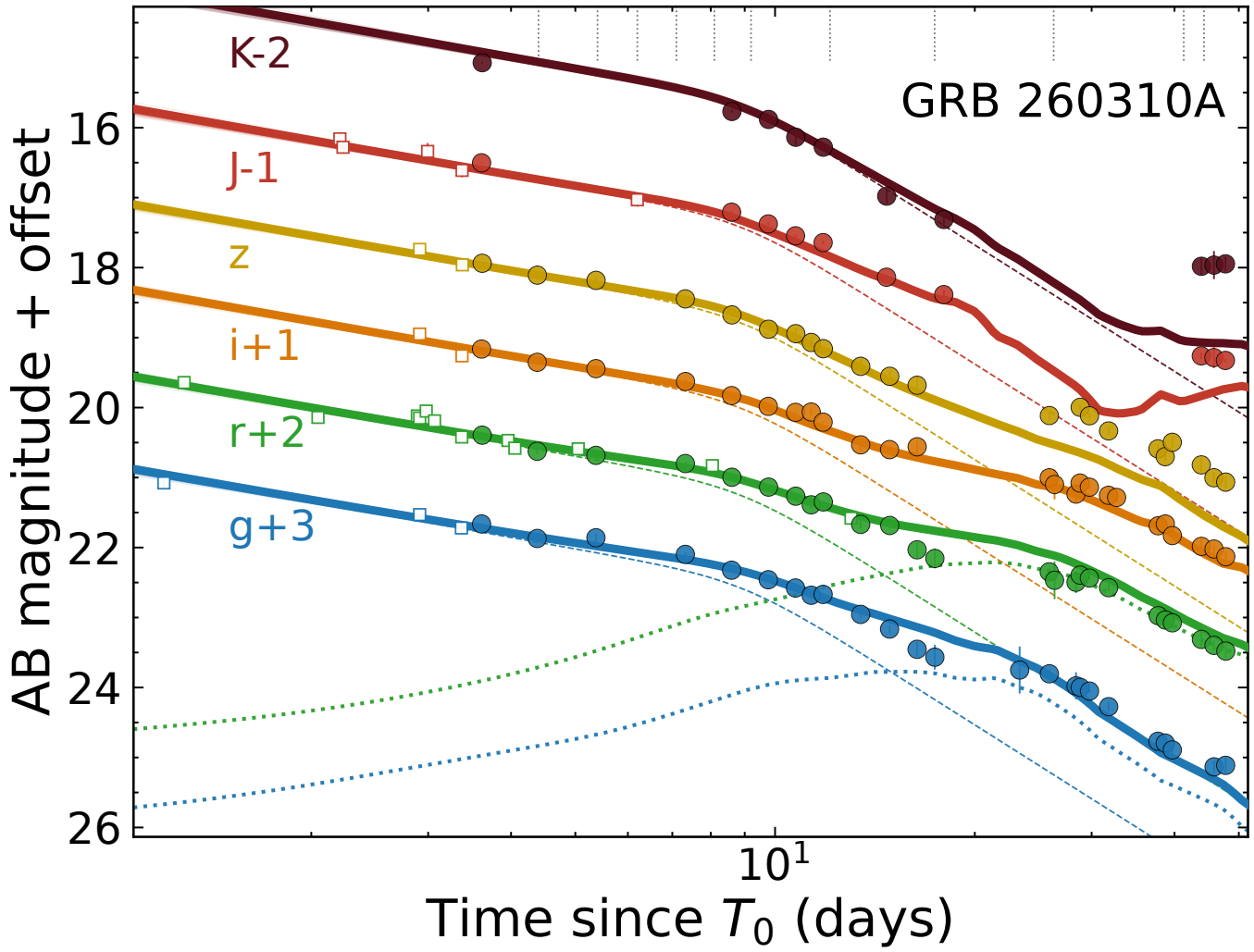


Figure 11. Best-fit model (power law + SN 1998bw) to the multiwavelength lightcurve of GRB 260310A in the observer frame. The thick solid lines in each filter represent the total model. The thin dashed lines represent the broken power-law afterglow component and the dotted lines, shown only in the *g* and *r* bands to avoid clutter, represent the model lightcurve of SN 1998bw with a flux scaling factor $k_{98bw} = 0.50$. Photometry presented in this work is shown as a solid circle and publicly reported photometry compiled from GCN Circulars is shown as empty squares (S. Belkin & M. Shrestha 2026; R. Brivio et al. 2026; K. Hinds et al. 2026; R. Konno et al. 2026; C.-H. Lai et al. 2026; J.-J. Li et al. 2026; A. Martin-Carrillo et al. 2026a, 2026b; E. Moreno Méndez et al. 2026; N. Passaleva et al. 2026; D. A. Perley et al. 2026; R. Stein et al. 2026; A. M. Watson et al. 2026).

ORCID iDs

Brendan O'Connor https://orcid.org/0000-0002-9700-0036
Malte Busmann https://orcid.org/0009-0001-0574-2332
Xander J. Hall https://orcid.org/0000-0002-9364-5419
Kenta Taguchi https://orcid.org/0000-0002-8482-8993
Masaomi Tanaka https://orcid.org/0000-0001-8253-6850
Daniel Gruen https://orcid.org/0000-0003-3270-7644
Seiji Toshikage https://orcid.org/0009-0002-5156-7819
Ariel J. Amsellem https://orcid.org/0000-0003-3433-2698
Ziyuan Zhu https://orcid.org/0009-0001-8023-5701
Antonella Palmese https://orcid.org/0000-0002-6011-0530
Dylan Green https://orcid.org/0000-0002-0676-3661
John Banovetz https://orcid.org/0000-0003-0776-8859
Yu-Han Yang https://orcid.org/0000-0003-0691-6688
Eleonora Troja https://orcid.org/0000-0002-1869-7817
Hendrik van Eerten https://orcid.org/0000-0002-8680-8718
Julius Gassert https://orcid.org/0009-0008-2754-1946
Mitra Maleki https://orcid.org/0009-0001-5050-6232
Stephen Bailey https://orcid.org/0000-0003-4162-6619
Segev BenZvi https://orcid.org/0000-0001-5537-4710
Tomás Cabrera https://orcid.org/0000-0002-1270-7666
Keerthi Kunnumkai https://orcid.org/0009-0000-4830-1484
Christoph Ries https://orcid.org/0009-0006-6697-8548
David Schlegel https://orcid.org/0000-0002-5042-5088
Michael Schmidt https://orcid.org/0009-0003-1323-9774
Muskan Yadav https://orcid.org/0009-0004-9520-5822

References

Aihara, H., Allende Prieto, C., An, D., et al. 2011, ApJS, 193, 29
Amati, L. 2006, MNRAS, 372, 233
Amati, L., Frontera, F., Tavani, M., et al. 2002, A&A, 390, 81
Arnett, W. D. 1982, ApJ, 253, 785
Ashall, C., Mazzali, P. A., Pian, E., et al. 2019, MNRAS, 487, 5824
Ashton, G., Hübner, M., Lasky, P. D., et al. 2019, ApJS, 241, 27
Asplund, M., Grevesse, N., Sauval, A. J., Allende Prieto, C., & Kiselman, D. 2004, A&A, 417, 751
Asplund, M., Grevesse, N., Sauval, A. J., & Scott, P. 2009, ARA&A, 47, 481
Astropy Collaboration, Price-Whelan, A. M., Lim, P. L., et al. 2022, ApJ, 935, 167

Astropy Collaboration, Price-Whelan, A. M., Sipőcz, B. M., et al. 2018, AJ, 156, 123
Astropy Collaboration, Robitaille, T. P., Tollerud, E. J., et al. 2013, A&A, 558, A33
Atteia, J.-L., Moreno Méndez, E., Lincetto, M., et al. 2026, GCN, 43981, 1
Baldwin, J. A., Phillips, M. M., & Terlevich, R. 1981, PASP, 93, 5
Barbary, K., Barclay, T., Biswas, R., et al. 2016, SNCosmo: Python library for SN cosmology, Astrophysics Source Code Library, ascl:1611.017
Belkin, S., & Shrestha, M. 2026, GCN, 44043, 1
Berger, E., Kulkarni, S. R., Pooley, G., et al. 2003, Natur, 426, 154
Bertin, E. 2006, ASPC, 351, 112
Bertin, E. 2010, SWarp: Resampling and Co-adding FITS Images Together, Astrophysics Source Code Library, ascl:1010.068
Bertin, E., & Arnouts, S. 1996, A&AS, 117, 393
Bertin, E., Mellier, Y., Radovich, M., et al. 2002, ASPC, 281, 228
Beuermann, K., Hessman, F. V., Reinsch, K., et al. 1999, A&A, 352, L26
Bhirombhakdi, K., Fruchter, A. S., Levan, A. J., et al. 2024, ApJ, 977, 256
Björnsson, C.-I., & Fransson, C. 2004, ApJ, 605, 823
Blanchard, P. K., Berger, E., & Fong, W.-f. 2016, ApJ, 817, 144
Blanchard, P. K., Villar, V. A., Chornock, R., et al. 2024, NatAs, 8, 774
Bloom, J. S., Kulkarni, S. R., & Djorgovski, S. G. 2002, AJ, 123, 1111
Bloom, J. S., Kulkarni, S. R., Djorgovski, S. G., et al. 1999, Natur, 401, 453
Bradley, L., Sipőcz, B., Robitaille, T., et al. 2024, astropy/photutils: 2.0.2,
Brivio, R., Malesani, D., Izzo, L., et al. 2026, GCN, 44004, 1
Bufano, F., Pian, E., Sollerman, J., et al. 2012, ApJ, 753, 67
Busmann, M., O'Connor, B., Sommer, J., et al. 2025, A&A, 701, A225
Campana, S., Mangano, V., Blustin, A. J., et al. 2006, Natur, 442, 1008
Cano, Z. 2013, MNRAS, 434, 1098
Cano, Z., Bersier, D., Guidorzi, C., et al. 2011, ApJ, 740, 41
Cano, Z., Izzo, L., de Ugarte Postigo, A., et al. 2017b, A&A, 605, A107
Cano, Z., Wang, S.-Q., Dai, Z.-G., & Wu, X.-F. 2017a, AdAst, 2017, 8929054
Cappellari, M. 2012, pPXF: Penalized Pixel-Fitting stellar kinematics extraction, Astrophysics Source Code Library, ascl:1210.002
Cappellari, M. 2017, MNRAS, 466, 798
Cappellari, M., & Emsellem, E. 2004, PASP, 116, 138
Chabrier, G. 2003, PASP, 115, 763
Chambers, K. C., Magnier, E. A., Metcalfe, N., et al. 2016, arXiv:1612.05560
Chen, T.-W., Aryan, A., Yang, S., et al. 2026, arXiv:2606.10009
Chevalier, R. A. 1982, ApJ, 259, 302
Chevalier, R. A., & Fransson, C. 2006, ApJ, 651, 381
Chonis, T. S., Hill, G. J., Lee, H., Tuttle, S. E., & Vattiat, B. L. 2014, SPIE, 9147, 91470A
Chonis, T. S., Hill, G. J., Lee, H., et al. 2016, SPIE, 9908, 99084C
Chornock, R., Berger, E., Levesque, E. M., et al. 2010, arXiv:1004.2262
Christensen, L., Vreeswijk, P. M., Sollerman, J., et al. 2008, A&A, 490, 45
Christy, C. T., Laskar, T., Alexander, K. D., et al. 2026, ApJL, 1006, L8
Clocchiatti, A., Suntzeff, N. B., Covarrubias, R., & Candia, P. 2011, AJ, 141, 163
Corcoran, G., Martin-Carrillo, A., Izzo, L., et al. 2026, GCN, 44105, 1
Cotter, L., Martin-Carrillo, A., Eyles-Ferris, R. A. J., et al. 2026, arXiv:2606.06213
de Ugarte Postigo, A., Geier, S., Izzo, L., et al. 2026a, GCN, 44124, 1
de Ugarte Postigo, A., Izzo, L., Martin-Carrillo, A., et al. 2026b, GCN, 43984, 1
de Ugarte Postigo, A., Izzo, L., Pugliese, G., et al. 2022, GCN, 32648, 1
de Ugarte Postigo, A., Thöne, C. C., Bensch, K., et al. 2018, A&A, 620, A190
de Ugarte Postigo, A., Thöne, C. C., Martín, S., et al. 2020, A&A, 633, A68
D'Elia, V., Campana, S., D'Aì, A., et al. 2018, A&A, 619, A66
D'Elia, V., Pian, E., Melandri, A., et al. 2015, A&A, 577, A116
Deng, J., Tominaga, N., Mazzali, P. A., Maeda, K., & Nomoto, K. 2005, ApJ, 624, 898
DESI Collaboration, Abdul-Karim, M., Adame, A. G., et al. 2026, AJ, 171, 285
DESI Collaboration, Abdul-Karim, M., Adame, A. G., et al. 2025, PhRvD, 112, 083515
DESI Collaboration, Adame, A. G., Aguilar, J., et al. 2024, AJ, 168, 58
DESI Collaboration, Aghamousa, A., Aguilar, J., et al. 2016, arXiv:1611.00037
Eyles-Ferris, R. A. J., Jonker, P. G., Levan, A. J., et al. 2025, ApJL, 988, L14
Fan, Y.-Z., Zhang, B.-B., Xu, D., Liang, E.-W., & Zhang, B. 2011, ApJ, 726, 32
Fermi GBM Team 2026, GCN, 43951, 1
Ferrero, P., Kann, D. A., Zeh, A., et al. 2006, A&A, 457, 857
Filippenko, A. V. 1982, PASP, 94, 715
Finneran, G., Cotter, L., & Martin-Carrillo, A. 2025, A&C, 52, 100954
Fruchter, A. S., Levan, A. J., Strolger, L., et al. 2006, Natur, 441, 463
Fulton, M. D., Smartt, S. J., Rhodes, L., et al. 2023, ApJL, 946, L22
Galama, T. J., Vreeswijk, P. M., van Paradijs, J., et al. 1998, Natur, 395, 670
Galama, T. J., Vreeswijk, P. M., van Paradijs, J., et al. 1999, A&AS, 138, 465
Gehrels, N., Chincarini, G., Giommi, P., et al. 2004, ApJ, 611, 1005
Giarratana, S., Giroletti, M., Ghirlanda, G., et al. 2026, GCN, 44045, 1
Gill, R., Becerra, R. L., de Ugarte Postigo, A., et al. 2026, arXiv:2605.26091
Gössl, C. A., & Riffeser, A. 2002, A&A, 381, 1095
Granot, J., Panaitescu, A., Kumar, P., & Woosley, S. E. 2002, ApJL, 570, L61
Granot, J., & Sari, R. 2002, ApJ, 568, 820
Greiner, J., Mazzali, P. A., Kann, D. A., et al. 2015, Natur, 523, 189
Guy, J., Bailey, S., Kremin, A., et al. 2023, AJ, 165, 144
Hall, X. J., Palmese, A., BenZvi, S., et al. 2026a, Zenodo,
Hall, X. J., Palmese, A., BenZvi, S., et al. 2026b, ApJS, 285, 10
Hall, X. J., Palmese, A., O'Connor, B., et al. 2026c, ApJL, 1001, L20
Hamburg, R., & Meegan, C. 2026, GCN, 43975, 1
Han, X. H., Hammer, F., Liang, Y. C., et al. 2010, A&A, 514, A24
Heintz, K. E., Malesani, D., Wiersema, K., et al. 2018, MNRAS, 474, 2738
Hill, G. J., Lee, H., MacQueen, P. J., et al. 2021, AJ, 162, 298
Hinds, K., Hall, X. J., Perley, D. A., et al. 2026, TNSAN, 65, 1
Hinds, K.-R., Perley, D. A., Ho, A. Y. Q., et al. 2026a, GCN, 43977, 1
Hinds, K.-R., Ho, A. Y. Q., Wagh, Y., et al. 2026b, arXiv:2606.05146
Hjorth, J. 2013, RSPTA, 371, 20120275
Hjorth, J., & Bloom, J. S. 2012, in Chapter 9 in "Gamma-Ray Bursts, ed. C. Kouveliotou, R. A. M. J. Wijers, & S. Woosley (Cambridge Univ. Press), 169
Hjorth, J., Sollerman, J., Møller, P., et al. 2003, Natur, 423, 847
Hopp, U., Bender, R., Grupp, F., et al. 2014, SPIE, 9145, 91452D
Hsu, B., Shrestha, M., Andrews, J., et al. 2026, GCN, 43986, 1
Hu, L., Wang, L., Chen, X., & Yang, J. 2022, ApJ, 936, 157
Hu, Y.-D., Castro-Tirado, A. J., Kumar, A., et al. 2021, A&A, 646, A50
Iwamoto, K., Mazzali, P. A., Nomoto, K., et al. 1998, Natur, 395, 672
Izzo, L., de Ugarte Postigo, A., Maeda, K., et al. 2019, Natur, 565, 324
Izzo, L., Martin-Carrillo, A., Malesani, D. B., et al. 2025, GCN, 39851, 1
Izzo, L., Thöne, C. C., Schulze, S., et al. 2017, MNRAS, 472, 4480
Jayaraman, R., Hinds, K.-R., Waratkar, G., et al. 2026a, GCN, 44234, 1
Jayaraman, R., Ho, A. Y. Q., Hinds, K.-R., et al. 2026b, GCN, 43994, 1
Jayaraman, R., Waratkar, G., Hinds, K.-R., et al. 2026c, GCN, 44095, 1
Kann, D. A., Klose, S., & Zeh, A. 2006, ApJ, 641, 993
Kann, D. A., Klose, S., Zhang, B., et al. 2010, ApJ, 720, 1513
Kann, D. A., Klose, S., Zhang, B., et al. 2011, ApJ, 734, 96
Kelly, P. L., Filippenko, A. V., Fox, O. D., Zheng, W., & Clubb, K. I. 2013, ApJL, 775, L5
Kennicutt, R. C. J. 1998, ARA&A, 36, 189
Klose, S., Schmidl, S., Kann, D. A., et al. 2019, A&A, 622, A138
Konno, R., Garrappa, S., Zimmerman, E. A., et al. 2026, GCN, 43974, 1
Kouveliotou, C., Woosley, S. E., Patel, S. K., et al. 2004, ApJ, 608, 872
Krühler, T., Kuncarayakti, H., Schady, P., et al. 2017, A&A, 602, A85
Krühler, T., Malesani, D., Fynbo, J. P. U., et al. 2015, A&A, 581, A125
Kulkarni, S. R., Frail, D. A., Wieringa, M. H., et al. 1998, Natur, 395, 663
Kumar, P., & Granot, J. 2003, ApJ, 591, 1075
Kumar, P., & Panaitescu, A. 2000, ApJL, 541, L51
Labrie, K., Anderson, K., Cárdenes, R., Simpson, C., & Turner, J. E. H. 2019, ASPC, 523, 321
Labrie, K., Simpson, C., Cardenes, R., et al. 2023, RNAAS, 7, 214
Lai, C.-H., Aryan, A., Lee, Y.-H., et al. 2026, GCN, 44002, 1
Lang-Bardl, F., Bender, R., Goessl, C., et al. 2016, SPIE, 9908, 990844
Laskar, T., Alexander, K. D., Margutti, R., et al. 2023, ApJL, 946, L23
Levan, A. J., Lamb, G. P., Schneider, B., et al. 2023, ApJL, 946, L28
Levesque, E. M., Berger, E., Kewley, L. J., & Bagley, M. M. 2010a, AJ, 139, 694
Levesque, E. M., Berger, E., Soderberg, A. M., & Chornock, R. 2011, ApJ, 739, 23
Levesque, E. M., Kewley, L. J., Berger, E., & Zahid, H. J. 2010b, AJ, 140, 1557
Li, J.-J., Chen, C., Cao, D.-L., et al. 2026, GCN, 43993, 1
Li, W. X., Zhu, Z. P., Zou, X. Z., et al. 2025, arXiv:2504.17034
Liang, E. W., Zhang, B., O'Brien, P. T., et al. 2006, ApJ, 646, 351
Lipkin, Y. M., Ofek, E. O., Gal-Yam, A., et al. 2004, ApJ, 606, 381
Lyman, J. D., Levan, A. J., Tanvir, N. R., et al. 2017, MNRAS, 467, 1795
Lyons, N., O'Brien, P. T., Zhang, B., et al. 2010, MNRAS, 402, 705
MacFadyen, A. I., & Woosley, S. E. 1999, ApJ, 524, 262
MacFadyen, A. I., Woosley, S. E., & Heger, A. 2001, ApJ, 550, 410
Malesani, D., Tagliaferri, G., Chincarini, G., et al. 2004, ApJL, 609, L5
Malesani, D. B., Levan, A. J., Izzo, L., et al. 2025, A&A, 701, A134
Margutti, R., Soderberg, A. M., Chomiuk, L., et al. 2012, ApJ, 751, 134
Margutti, R., Soderberg, A. M., Wieringa, M. H., et al. 2013, ApJ, 778, 18
Marino, R. A., Rosales-Ortega, F. F., Sánchez, S. F., et al. 2013, A&A, 559, A114

Martin-Carrillo, A., Aasen, E., Brown, L., et al. 2026a, GCN, 44000, 1
Martin-Carrillo, A., Roca Garcia-Valino, J., Aasen, E., et al. 2026b, GCN, 43979, 1
Martin-Carrillo, A., Thöne, C. C., Leung, J. K., et al. 2026c, arXiv:2606.10002
Maselli, A., Melandri, A., Nava, L., et al. 2014, Sci, 343, 48
Matheson, T., Garnavich, P. M., Stanek, K. Z., et al. 2003, ApJ, 599, 394
Matsubayashi, K., Ohta, K., Iwamuro, F., et al. 2019, PASJ, 71, 102
Matsubayashi, K., Tsutsui, H., Nakaya, H., et al. 2025, PASJ, 77, 1065
Mazzali, P. A., Pian, E., Bufano, F., & Ashall, C. 2021, MNRAS, 505, 4106
Mazzali, P. A., Deng, J., Nomoto, K., et al. 2006, Natur, 442, 1018
Mazzali, P. A., Deng, J., Tominaga, N., et al. 2003, ApJL, 599, L95
McKenzie, E. H., & Schaefer, B. E. 1999, PASP, 111, 964
Melandri, A., Malesani, D. B., Izzo, L., et al. 2019, MNRAS, 490, 5366
Mészáros, P., & Rees, M. J. 1999, MNRAS, 306, L39
MichałowskI, M. J., Xu, D., Stevens, J., et al. 2018, A&A, 616, A169
Miller, T. N., Doel, P., Gutierrez, G., et al. 2024, AJ, 168, 95
Moreno Méndez, E., Lincetto, M., Dornic, D., et al. 2026, GCN, 43980, 1
Myers, A. D., Moustakas, J., Bailey, S., et al. 2023, AJ, 165, 50
Nicuesa Guelbenzu, A., Klose, S., Greiner, J., et al. 2012, A&A, 548, A101
O'Connor, B., Hall, X. J., Busmann, M., et al. 2026a, ApJL, 1006, L13
O'Connor, B., Toshikage, S., Tanaka, M., et al. 2026b, GCN, 44137, 1
O'Connor, B., Troja, E., Ryan, G., et al. 2023, SciA, 9, eadi1405
Olivares, E. F., Greiner, J., Schady, P., et al. 2012, A&A, 539, A76
O'Neill, D., Ramsay, G., Ackley, K., et al. 2026, TNSTR, 2026-1001, 1
Osterbrock, D. E. 1989, Astrophysics of Gaseous Nebulae and Active Galactic Nuclei (Univ. Science Books)
Panaitescu, A., & Kumar, P. 2003, ApJ, 592, 390
Passaleva, N., Yang, Y.-H., Shahamt, N., Troja, E. & ERC BHianca Team 2026, GCN, 44058, 1
Patat, F., Cappellaro, E., Danziger, J., et al. 2001, ApJ, 555, 900
Pedersen, H., Jaunsen, A. O., Grav, T., et al. 1998, ApJ, 496, 311
Peng, F., Königl, A., & Granot, J. 2005, ApJ, 626, 966
Perley, D. A., Cenko, S. B., Corsi, A., et al. 2014, ApJ, 781, 37
Perley, D. A., Wagh, Y., Jayaraman, R., et al. 2026, GCN, 44096, 1
Pettini, M., & Pagel, B. E. J. 2004, MNRAS, 348, L59
Pian, E., Mazzali, P. A., Masetti, N., et al. 2006, Natur, 442, 1011
Piran, T. 2004, RvMP, 76, 1143
Planck Collaboration, Aghanim, N., Akrami, Y., et al. 2020, A&A, 641, A6
Poppett, C., Tyas, L., Aguilar, J., et al. 2024, AJ, 168, 245
Ramsey, L. W., Adams, M. T., Barnes, T. G., et al. 1998, SPIE, 3352, 34
Rastinejad, J. C., Levan, A. J., Jonker, P. G., et al. 2025, ApJL, 988, L13
Rastinejad, J. C., Srinivasaragavan, G., Sarin, N., et al. 2026, arXiv:2606.10011
Rees, M. J., & Mészáros, P. 1998, ApJL, 496, L1
Rhoads, J. E. 1999, ApJ, 525, 737
Rhoads, J. E., & Fruchter, A. S. 2001, ApJ, 546, 117
Rhodes, L., Hughes, A., Fender, R., et al. 2026, GCN, 44005, 1
Rossi, A., Izzo, L., Maeda, K., et al. 2026, A&A, 708, A60
Rossi, E., Lazzati, D., & Rees, M. J. 2002, MNRAS, 332, 945
Rowlinson, A., O'Brien, P. T., Tanvir, N. R., et al. 2010, MNRAS, 409, 531
Salunke, S., Harsha, K. H., Tembhurnikar, M., et al. 2026, GCN, 43958, 1
Sari, R., & Mészáros, P. 2000, ApJL, 535, L33
Sari, R., Piran, T., & Halpern, J. P. 1999, ApJL, 519, L17
Sari, R., Piran, T., & Narayan, R. 1998, ApJL, 497, L17
Sarin, N., Hübner, M., Omand, C. M. B., et al. 2024, MNRAS, 531, 1203
Schlafly, E. F., & Finkbeiner, D. P. 2011, ApJ, 737, 103
Schlafly, E. F., Kirkby, D., Schlegel, D. J., et al. 2023, AJ, 166, 259
Schulze, S., Malesani, D., Cucchiara, A., et al. 2014, A&A, 566, A102
Sheth, K., Frail, D. A., White, S., et al. 2003, ApJL, 595, L33
Shetrone, M., Cornell, M. E., Fowler, J. R., et al. 2007, PASP, 119, 556
Shrestha, M., Sand, D. J., Alexander, K. D., et al. 2023, ApJL, 946, L25
Skrutskie, M. F., Cutri, R. M., Stiening, R., et al. 2006, AJ, 131, 1163
Soderberg, A. M., Kulkarni, S. R., Nakar, E., et al. 2006, Natur, 442, 1014
Soderberg, A. M., Margutti, R., Zauderer, B. A., et al. 2012, ApJ, 752, 78
Sollerman, J., Holland, S. T., Challis, P., et al. 2002, A&A, 386, 944
Sollerman, J., Jaunsen, A. O., Fynbo, J. P. U., et al. 2006, A&A, 454, 503
Sollerman, J., Kozma, C., Fransson, C., et al. 2000, ApJL, 537, L127
Speagle, J. S. 2020, MNRAS, 493, 3132
Srinivasaragavan, G. P., Hamidani, H., Schroeder, G., et al. 2025a, ApJL, 988 (2) L60
Srinivasaragavan, G. P., Li, D., Hall, X. J., et al. 2025b, arXiv:2512.10239
Srinivasaragavan, G. P., O'Connor, B., Cenko, S. B., et al. 2023, ApJL, 949, L39
Stampoulis, V., van Dyk, D. A., Kashyap, V. L., & Zezas, A. 2019, MNRAS, 485, 1085
Stanek, K. Z., Matheson, T., Garnavich, P. M., et al. 2003, ApJL, 591, L17
Stanway, E. R., Levan, A. J., Tanvir, N., et al. 2015, MNRAS, 446, 3911
Starling, R. L. C., Wiersema, K., Levan, A. J., et al. 2011, MNRAS, 411, 2792
Stathakis, R. A., Boyle, B. J., Jones, D. H., et al. 2000, MNRAS, 314, 807
Stein, R., Mo, G., Karambelkar, V., et al. 2026, GCN, 43996, 1
Tanga, M., Krühler, T., Schady, P., et al. 2018, A&A, 615, A136
Taylor, G. B., Frail, D. A., Berger, E., & Kulkarni, S. R. 2004, ApJL, 609, L1
Thöne, C. C., Christensen, L., Prochaska, J. X., et al. 2014, MNRAS, 441, 2034
Thöne, C. C., Izzo, L., Flores, H., et al. 2021, A&A, 656, A136
Thöne, C. C., de Ugarte Postigo, A., Izzo, L., et al. 2024, A&A, 690, A66
Toy, V. L., Cenko, S. B., Silverman, J. M., et al. 2016, ApJ, 818, 79
Troja, E., Cusumano, G., O'Brien, P. T., et al. 2007, ApJ, 665, 599
van der Horst, A. J., Kamble, A., Resmi, L., et al. 2008, A&A, 480, 35
Vanderspek, R., Sakamoto, T., Barraud, C., et al. 2004, ApJ, 617, 1251
Vazdekis, A., Koleva, M., Ricciardelli, E., Röck, B., & Falcón-Barroso, J. 2016, MNRAS, 463, 3409
Vestrand, W. T., Wren, J. A., Panaitescu, A., et al. 2014, Sci, 343, 38
Vincenzi, M., Sullivan, M., Firth, R. E., et al. 2019, MNRAS, 489, 5802
Volnova, A. A., Pruzhinskaya, M. V., Pozanenko, A. S., et al. 2017, MNRAS, 467, 3500
Wang, J., Zhu, Z. P., Xu, D., et al. 2018, ApJ, 867, 147
Waratkar, G., Kammoun, E., Jayaraman, R., Hinds, K.-R., & Ho, A. Y. Q. 2026, GCN, 44278, 1
Watson, A. M., Dornic, D., Becerra, R. L., et al. 2026, GCN, 44001, 1
Wijers, R. A. M. J., & Galama, T. J. 1999, ApJ, 523, 177
Woosley, S. E. 1993, ApJ, 405, 273
Woosley, S. E., & Bloom, J. S. 2006, ARA&A, 44, 507
Xu, D., de Ugarte Postigo, A., Leloudas, G., et al. 2013, ApJ, 776, 98
Yang, Y.-H., Ricci, R., Troja, E., et al. 2026, arXiv:2605.23818
York, D. G., Adelman, J., Anderson, J. E., Jr., et al. 2000, AJ, 120, 1579
Yuan, W., Dai, L., Feng, H., et al. 2025, SCPMA, 68, 239501
Yuan, W., Huang, Q.-J., Zhu, J.-P., et al. 2026, arXiv:2606.10014
Zeh, A., Klose, S., & Hartmann, D. H. 2004, ApJ, 609, 952
Zhang, B., Fan, Y. Z., Dyks, J., et al. 2006, ApJ, 642, 354
Zhang, B., & Mészáros, P. 2001, ApJL, 552, L35